

Intrinsic Alignment in redMaPPer clusters – II. Radial alignment of satellites toward cluster centers

Hung-Jin Huang¹^{*}, Rachel Mandelbaum¹[†], Peter E. Freeman^{1,2}, Yen-Chi Chen³, Eduardo Rozo⁴ & Eli Rykoff⁵

¹*McWilliams Center for Cosmology, Department of Physics, Carnegie Mellon University, Pittsburgh, PA 15213, USA*

²*Department of Statistics, Carnegie Mellon University, Pittsburgh, PA 15213, USA*

³*Department of Statistics, University of Washington, Seattle, WA 98195, USA*

⁴*Department of Physics, University of Arizona, 1118 E. Fourth St., Tucson, AZ 85721, USA*

⁵*SLAC National Accelerator Laboratory, Menlo Park, CA 94025, USA*

Accepted XXX. Received YYY; in original form ZZZ

ABSTRACT

We study the orientations of satellite galaxies in redMaPPer clusters constructed from the Sloan Digital Sky Survey at $0.1 < z < 0.35$ to determine whether there is any preferential tendency for satellites to point radially toward cluster centers. We analyze the satellite alignment (SA) signal based on three shape measurement methods (re-Gaussianization, de Vaucouleurs, and isophotal shapes), which trace galaxy light profiles at different radii. The measured SA signal depends on these shape measurement methods. We detect the strongest SA signal in isophotal shapes, followed by de Vaucouleurs shapes. While no net SA signal is detected using re-Gaussianization shapes across the entire sample, the observed SA signal reaches a statistically significant level when limiting to a subsample of higher luminosity satellites. We further investigate the impact of noise, systematics, and real physical isophotal twisting effects in the comparison between the SA signal detected via different shape measurement methods. Unlike previous studies, which only consider the dependence of SA on a few parameters, here we explore a total of 17 galaxy and cluster properties, using a statistical model averaging technique to naturally account for parameter correlations and identify significant SA predictors. We find that the measured SA signal is strongest for satellites with the following characteristics: higher luminosity, smaller distance to the cluster center, rounder in shape, higher bulge fraction, and distributed preferentially along the major axis directions of their centrals. Finally, we provide physical explanations for the identified dependences, and discuss the connection to theories of SA.

Key words: galaxies: clusters: general – large-scale structure of Universe

1 INTRODUCTION

The projected orientations of galaxies observed on sky are not random, but rather exhibit some coherent patterns related to the matter distribution in the Universe. Galaxy shapes tend to point towards overdense regions, leaving a net preference of correlated orientations. This phenomenon, known as “intrinsic” alignments (IA), contains important information about structure formation and galaxy evolution (for recent reviews, see [Joachimi et al. 2015](#); [Kirk et al.](#)

[2015](#); [Kiessling et al. 2015](#)). Besides the physically-induced alignment signal, the images of galaxies located behind overdense structures tend to be distorted tangentially with respect to those structures, producing the apparent tangential alignment signal that is the key characteristic of gravitational lensing. This lensing effect is used as a tool to map the distribution of dark matter in the Universe, to study the growth of structure, and to constrain cosmological parameters (see e.g. [Massey et al. 2010](#); [Weinberg et al. 2013](#); [Mandelbaum et al. 2013](#)). The presence of IA challenges the process of interpreting the observed shape correlations (intrinsic+apparent) in terms of the basic physics that generates lensing signals. Ongoing surveys such as the Dark

^{*} E-mail: hungjinh@andrew.cmu.edu

[†] E-mail: rmandelb@andrew.cmu.edu

Energy Survey (DES, [Dark Energy Survey Collaboration et al. 2016](#)), the Kilo-Degree Survey (KiDS, [de Jong et al. 2015](#)), Hyper Suprime-Cam Survey (HSC, [Miyazaki et al. 2012](#)), and future surveys like the Large Synoptic Survey Telescope (LSST, [LSST Science Collaboration et al. 2009](#)), Euclid ([Laureijs et al. 2011](#)), and the Wide Field Infrared Survey Telescope (WFIRST, [Spergel et al. 2015](#)) aim to constrain the cosmological constants to sub-percent precision, which requires precise removal of all possible systematics including intrinsic alignments (e.g., [Blazek et al. 2012](#); [Krause et al. 2016](#)). Quantifying the strength of IA signal and developing models that will enable its removal thus becomes one of the key steps to reach this goal.

IA have been detected over a wide range of scales. On scales above several Mpc, red dispersion-dominated galaxies preferentially point towards overdense regions (see e.g., [Mandelbaum et al. 2006](#); [Hirata et al. 2007](#); [Okumura et al. 2009](#); [Joachimi et al. 2011](#); [Singh et al. 2015](#) from the observational side, and [Tenneti et al. 2015](#); [Chisari et al. 2015](#) from numerical simulation). Part of this observed correlation originates from the tendency of galaxies to align towards overdensities and with filamentary structures (see e.g., observation: [Zhang et al. 2013](#); [Tempel et al. 2015](#), and simulation: [Chen et al. 2015](#)). For red galaxies located in sheets, [Zhang et al. \(2013\)](#) observed that they tend to have their major axes aligned parallel to the plane of the sheets. For blue angular momentum-dominated galaxies, there is no significant detection of alignment so far ([Mandelbaum et al. 2011](#)). Besides the alignment of galaxies, people also found alignment between the shape of clusters with respect to the underlying density field (observation: [Smargon et al. 2012](#); [van Uitert & Joachimi 2017](#); simulation: [Hopkins et al. 2005](#)).

The other alignment at intra-halo scale is satellite alignment, i.e. the preference of satellites to align radially toward the cluster center. The SA signal is relatively subtle compared with the strength of central galaxy alignment; along with the difficulty of achieving accurate shape measurements on faint satellites whose light profiles are more subject to contamination from neighboring galaxies, many conflicting observational results have been published. Earlier works based on SDSS isophotal shape measurement, which trace the very outer part of the galaxy light profiles, have reported detections of SA signal ([Pereira & Kuhn 2005](#); [Agustsson & Brainerd 2006](#); [Faltenbacher et al. 2007](#)). However, later studies claimed that when using de Vaucouleurs shape, which puts relatively more weight on the galaxy inner light profiles, satellite orientations are consistent with random ([Siverd et al. 2009](#); [Hao et al. 2010](#)). Studies that used shape measurements that are optimized for lensing, which requires corrections for many observational systematics, reported non-detection of satellite alignments ([Schneider et al. 2013](#); [Sifón et al. 2015](#)). There is therefore some tension between past measurements, and reconciliation of that tension may require investigation into the different galaxy populations used for these measurements and/or false SA signals generated by systematics in isophotal shape measurements (e.g., [Hao et al. 2010](#)).

Our current theoretical understanding of IA for red dispersion-dominated galaxies is that their orientations are affected by the tidal field of the surrounding environment. On large scales, the linear alignment model ([Catelan et al. 2001](#); [Hirata & Seljak 2004](#)) suggests that the shapes of

proto-galaxies are largely set by the primordial tidal field at their formation time, so that their shape correlation with the matter field is frozen in since then and simply grows with the matter power spectrum. The primordial tidal field also leaves its imprint on the assembly history of clusters by channeling the majority of satellites into clusters through accretion along filamentary structures, which results in the observed cluster alignment phenomenon ([Hopkins et al. 2005](#)). At small scales, the orientation of cluster central galaxies would also be generated by the same primordial tidal field, leaving the observed central galaxy alignment (see discussions in Paper I). While later non-linear evolutionary processes such as mergers or baryonic feedback from galaxies may erase the alignment signals set by primordial tidal fields ([Tenneti et al. 2017](#)), the late-time re-arranged structures can set up new tidal environments that gradually torque galaxies to align ([Ciotti & Dutta 1994](#); [Kuhlen et al. 2007](#); [Pereira et al. 2008](#); [Faltenbacher et al. 2008](#)). The timescales for tidal locking of satellites under the cluster potential depend on the eccentricity of infalling orbits as well as properties of satellites (e.g. angular momentum, morphology). As shown in the simulations of [Pereira & Bryan \(2010\)](#), within the time of one orbital period (~ 5 Gyr), a triaxial DM subhalo orbiting in circular orbit around a cluster potential becomes tidally locked, and it takes a lag of $\lesssim 2$ Gyr, depending on the initial conditions, for the stellar components to respond.

In this work, we carry out SA measurements using re-Gaussianization, de Vaucouleurs and isophotal shapes that differ in sensitivity to the outskirts of a galaxy’s light profile. The size of the redMaPPer cluster catalogue provides the necessary statistical power to constrain SA signals at halo masses $\gtrsim 10^{14} M_{\odot} h^{-1}$. The two main questions we aim to address in this paper are 1) What causes the detected discrepancies in SA signals using different shape measurement methods? 2) Which satellite properties associated with which central galaxy and cluster properties are correlated with stronger SA signals? We estimate the level of possible noises and systematics that could cause the inconsistent galaxy position angle (PA) measurements. As in paper I, we explore a large parameter pool which contains characteristic satellite, central galaxy, and cluster properties to identify important predictors of SA effect using linear regression analysis.

The paper is organized as follows. In Sec. 2, we describe our data and definitions of the physical parameters involved in the analysis. Sec. 3 presents the overall signal of SA alignment measured in redMaPPer clusters. Details of the linear regression and variable selection results are described in Sec. 4. Sec. 5 explores possible factors that cause the discrepancy in the measured SA angle using three different shape measurement methods, and provides estimates of the degree of contribution from each factor. The physical origins of our identified featured predictors on the SA effect are discussed in Sec. 6. We conclude and summarize our key findings in Sec. 7.

Throughout this paper, we adopt the standard flat Λ CDM cosmology with $\Omega_m = 0.3$ and $\Omega_{\Lambda} = 0.7$. All length and magnitude units use $H_0 = 100 \text{ km s}^{-1} \text{ Mpc}^{-1}$. We use log as shorthand for the 10-based logarithm.

2 DATA AND MEASUREMENTS

All data used in this paper come from the SDSS (York et al. 2000) surveys. Here we describe the catalogs involved in our analysis, sample construction, and definitions of the cluster- and galaxy-related parameters. Most of the data and parameters remain the same as in Paper I, although some small differences exist, as we will highlight in the relevant subsections below. In order to properly interpret the measured satellite alignments, Paper II puts more focus on exploring systematics in the different shape measurement approaches. New samples for systematic tests are constructed and described below.

2.1 Galaxy cluster catalog

Our cluster member galaxy sample is taken from the SDSS DR8 (Aihara et al. 2011) redMaPPer v5.10 cluster catalog¹, constructed based on a red-sequence cluster finding approach. Details of the algorithm and the cluster properties can be found in Rykoff et al. (2014); Rozo & Rykoff (2014); Rozo et al. (2015a,b). Some features of the redMaPPer cluster catalog are briefly summarized here.

For each cluster, it identifies five most probable central galaxies, with their corresponding central probability, P_{cen} . Each cluster member galaxy is assigned with a membership probability, p_{mem} , according to its color, magnitude, and position information. The photometric redshift z for each cluster is estimated from high-probability members. The cluster sample is approximately volume-limited in the redshift range of $0.1 \leq z \leq 0.35$. The cluster richness, λ , is defined by summing the membership probabilities over all possible cluster members. Most of the clusters have $\lambda \gtrsim 20$, corresponding to an approximate halo mass threshold of $M_{200\text{m}} \gtrsim 10^{14} h^{-1} M_{\odot}$ (Rykoff et al. 2012; Simet et al. 2017).

2.2 Galaxy shapes

2.2.1 Shape-related parameters

We adopt the following definition of ellipticity/distortion components in a global Cartesian frame to measure each galaxy's ellipticity:

$$(e_1, e_2) = \frac{1 - (b/a)^2}{1 + (b/a)^2} (\cos 2\alpha, \sin 2\alpha), \quad (1)$$

where b/a is the minor-to-major axis ratio and α the position angle (PA) of the major axis of the galaxy. Here e_1 measures the projected distortion in the RA/dec directions, and e_2 in diagonal directions. The total galaxy ellipticity e can then be calculated as

$$e = \sqrt{e_1^2 + e_2^2} = \frac{1 - (b/a)^2}{1 + (b/a)^2}. \quad (2)$$

Once the PA α of a galaxy is obtained by one of the methods described in Sec. 2.2.2, we can then derive its central galaxy alignment angle θ_{cen} and satellite alignment angle ϕ_{sat} as illustrated in Fig. 1.

The central galaxy alignment angle (θ_{cen}) is defined as the angle between the major axis of the central galaxy and

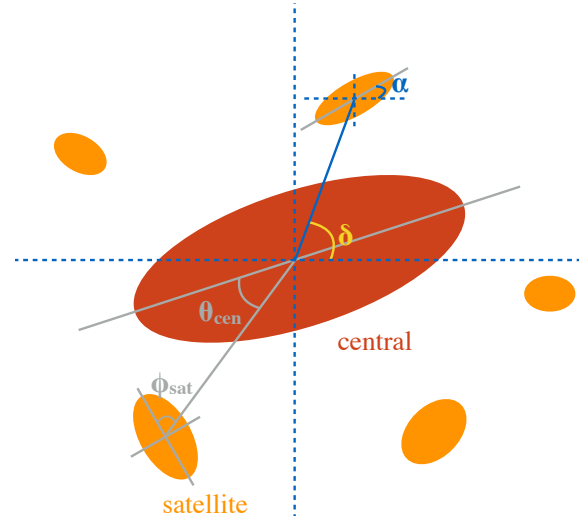


Figure 1. Illustration of the galaxy alignment angles. The satellite alignment angle, ϕ_{sat} , defined as the angle between a satellite's major axis and its orientation towards the central galaxy, is the main focus of this paper. The central galaxy alignment angle, θ_{cen} , defined as the angular location of a satellite relative to its central galaxy's major axis direction, is the area of focus in our previous Paper I.

the line connecting the central to the satellite galaxy. We only need a viable shape measurement for the central galaxy (but not the satellites) to derive θ_{cen} . The analysis of central galaxy alignments in redMaPPer clusters has already been reported in Paper I. The satellite alignment angle (ϕ_{sat}) is defined as the angle between the major axis of the satellite galaxy and the line connecting its center to the central galaxy. Deriving ϕ_{sat} requires a shape measurement for the satellite galaxy. In this paper, we focus on the satellite alignments, and will use the central galaxy alignment angle θ_{cen} as one of the candidate predictors in our parameter pool. We use the highest-probability centrals provided in redMaPPer for calculation of both θ_{cen} and ϕ_{sat} .

We restrict both θ_{cen} and ϕ_{sat} to the range $[0^\circ, 90^\circ]$ due to symmetry. By definition, $\theta_{\text{cen}} = 0^\circ/90^\circ$ indicates a satellite located along the major/minor axis of the central. A satellite is radially/tangentially aligned with the central if $\phi_{\text{sat}} = 0^\circ/90^\circ$.

Besides using ϕ_{sat} to quantify the degree of SA signal, another commonly-used parameter is e_+ , the distortion in the radial-tangential direction in a new frame with the original axes rotated to the radial-tangential directions of each central-satellite pair. From simple algebra, we have:

$$(e_+, e_x) = \frac{1 - (b/a)^2}{1 + (b/a)^2} (\cos 2(\delta - \alpha), \sin 2(\delta - \alpha)), \quad (3)$$

where α is the PA of the satellite, and δ the azimuthal angle of the satellite projected position with respect to the cluster central galaxy, as indicated in Fig. 1. A positive e_+ indicates a radial alignment of the satellite toward cluster center, while a negative e_+ indicates a tangential alignment. Therefore, if satellite galaxies do preferentially align in the radial direction, we expect $\langle e_+ \rangle > 0$ when taking the average over all central-satellite pairs. The e_x component is the distortion at $\pm 45^\circ$ from the radial/tangential direction. It is is

¹ <http://risa.stanford.edu/redmapper/>

commonly used as an indicator for certain systematics. Due to symmetry, $\langle e_x \rangle$ should be consistent with zero.

2.2.2 Shape data

We will measure satellite alignments using three shape measurement methods: re-Gaussianization, isophotal, and de Vaucouleurs shapes, to compare differences in the signals and investigate systematics. Details of these methods have been described in Paper I (Sec. 2.3), and we only briefly summarize here.

The re-Gaussianization shape measurement method (Hirata & Seljak 2003) is specifically designed for weak lensing studies, which require great care in removing the point spread function (PSF) effect on the observed galaxy images. This method has a Gaussian weight function that emphasizes the inner, brighter regions of galaxy profiles in order to reach higher precision distortion measurement especially for faint galaxies. In this work, we take the distortion measurement (e_1 and e_2) from a re-Gaussianization shape catalog of Reyes et al. (2012) with shapes measured in the r and i bands based on the SDSS DR8 photometry.

Isophotal shape measurement does not include an explicit correction for the effect of the PSF. It determines a galaxy’s shape by fitting the surface brightness at 25 mag/arcsec², which traces the outer part of a galaxy’s profile. Since isophotal shapes were not released in DR8, we take the isophotal position angle in r band from DR7 to compute satellite alignment angles.

The de Vaucouleurs shape measurements were determined by fitting each galaxy’s image with a de Vaucouleurs model (Stoughton et al. 2002), which is a good description for typical elliptical galaxies (which includes the majority of the galaxies in this work, since they were selected based on a red-sequence method). It partially corrects for the PSF effect using an approximate PSF model, and overall is sensitive to light profiles on scales between those measured by re-Gaussianization and isophotal methods. We use the de Vaucouleurs fit position angle in r band provided from the SDSS DR7 in this work ².

2.3 The central-satellite pair sample

To fairly compare the measured alignment signal across redshift, we restrict our analysis to a volume-limited cluster sample within $0.1 \leq z \leq 0.35$ from the redMaPPer catalog. Besides this, an appropriate membership probability cut of $p_{\text{mem}} \geq 0.55$ is applied on satellite galaxies, which results in a total of 305997 central-satellite pairs in 10749 distinct clusters (before requiring galaxies to have shape measurements). The choice of the $p_{\text{mem}} = 0.55$ cut comes from optimizing the S/N for detection of SA signals, as explained in Appendix A.

While applying a lower p_{mem} cut returns us more central-satellite pairs into analysis, the resulting satellite

alignment signal will be diluted due to the inclusion of more pairs with “satellite” galaxies that are not actually in clusters. Throughout this work, we will reduce this contamination by applying p_{mem} as the weighting factor on each central-satellite pair.

We define two sets of central-satellite pair samples for analysis in this work.

(i) **DR8 footprint sample:** The first set is within the SDSS DR8 footprint, constructed by acquiring that the 305997 $p_{\text{mem}} \geq 0.55$ satellites have well-defined re-Gaussianization shape measurements. There are 174180 central-satellite pairs within 8121 distinct clusters in this data set. The effective total number of pairs in DR8 footprint sample after weighting by p_{mem} is $\sum_i p_{\text{mem},i} \approx 132072$ pairs.

(ii) **DR7 footprint sample:** The second data set is constructed for comparing the level of satellite alignment signals via three different shape measurement methods. We require satellites in this subsample to have all three kinds of shape measurements, and thus this data set covers the smaller DR7 footprint. In total, there are 158537 central-satellite pairs within 7385 distinct clusters, or effectively 120200 after weighting by p_{mem} .

The resulting redshift and luminosity distributions of satellites in the constructed DR8 and DR7 sample sets are almost indistinguishable, indicating that the selection functions for different shape measurements are quite similar.

In Paper I, to investigate the effect of the sky-subtraction technique on the measured central galaxy alignment signal, we have reported the results based on a set of DR4 footprint satellites, which have re-Gaussianization shape measurement based on both DR4 and DR8 SDSS photometric pipelines. We found that within error bars, the measured central galaxy alignment signals are very similar when different photometric pipelines are used, and therefore concluded that the effect of sky-subtraction does not substantially influence the central galaxy alignment measurement. In this work for satellite alignment, we have also examined whether sky-subtraction is an issue for the detecting signal using the DR4 footprint data set, but did again failed to find any disagreement. For this reason, to simplify the analysis we will only report the measured satellite alignment results for the DR8 and DR7 footprint sample.

2.4 Systematic test sample

We construct three systematic test samples to study potential systematic effects in the crowded cluster environment. All of the samples are constructed from the redsequence Matched filter Galaxy v6.3 Catalog (redMaGiC) (Rozo et al. 2016), a photometrically-selected luminous red galaxy (LRG) catalog with very high quality photo- z estimation based on the SDSS DR8 photometric data. Overall, the bias, defined as the median value of $z_{\text{photo}} - z_{\text{spect}}$, of the DR8 redMaGiC photo- z is less than 0.005. The 1σ scatter of $(z_{\text{photo}} - z_{\text{spect}})/(1 + z_{\text{spect}})$ is $\lesssim 0.02$.

(i) **Foreground & background of redMaPPer:** The foreground and background sample is composed of galaxies that are in the same sky area as redMaPPer clusters, but

² We have tried fixing the shape measurement method to re-Gaussianization but varying SDSS photometry pipeline between DR4 and DR8. We found that the derived shape parameters based on different pipelines are statistically consistent. Similarly, we expect that using DR7 photometry for de Vaucouleurs shapes should give consistent results as using those based on DR8.

are not physically associated with the cluster. This sample is constructed as follows. For each central galaxy in the redMaPPer cluster, we use $1.5R_c(\lambda)$ as a searching radius to select out LRGs within the projected area in the redMaGiC catalog. The $R_c(\lambda)$ is the radius within which p_{mem} is assigned in the original redMaPPer catalog, and it is estimated that $R_{200c} \approx 1.5R_c(\lambda)$ (Rykoff et al. 2012, 2014). Next we select LRGs whose photo- $z < (>) z_{\text{cluster}}$ as foreground (background) candidates. To improve the purity of the sample, we further exclude $p_{\text{mem}} > 0.2$ galaxies in the “ubermem” version of the redMaPPer catalog. This “ubermem” catalog extends the p_{mem} estimation out to $1.5R_c(\lambda)$ and down to fainter galaxies ($\text{mag } i < 21$), thus enabling us to remove potential cluster members at $1 \sim 1.5R_c(\lambda)$ and those that are relatively faint, unlike in the original redMaPPer catalog. After this cut, 95% of foregrounds and 99% of backgrounds have their $\Delta z = |z_{\text{photo}} - z_{\text{cluster}}| \gtrsim 0.02$, suggesting that the above procedures return a set of clean foreground and background galaxies. After requiring these galaxies to have re-Gaussianization shape measurements, we have 45030 fake central-satellite pairs in the DR8 footprint, of which 4459 and 40571 are foreground and background galaxies, respectively. Further requiring these galaxies to have de Vaucouleurs and isophotal shapes in DR7, leaves us with 4134 and 36941 foreground and background galaxies, respectively.

(ii) **Non-cluster field sample:** To highlight the effect of the crowded cluster environment on the shape measurement of galaxies within the cluster area on the sky (either physically-associated member galaxies or just foreground/background galaxies), we construct a sample of galaxies that are not in the footprint of redMaPPer cluster fields, and call it the “non-cluster field sample”. We do so by simply taking the full redMaGiC catalog, and excluding all galaxies ($p_{\text{mem}} \geq 0$) that belong to the redMaPPer cluster member sample as well as galaxies in the foreground and background sample constructed above. After requiring that these galaxies have all three shape measurements, we have 697308 galaxies within the DR7 footprint.

(iii) **Foreground & background of $m_r < 19$ non-cluster field bright galaxies:** In order to understand the level of contamination caused by the extended light profile of bright central galaxies on nearby satellites, we select bright galaxies with $m_r < 19$ from our non-cluster field sample described above, and construct a sample composed of the corresponding foreground and background galaxies around these bright galaxies. We again find the foreground/background galaxies from redMaGiC, and require their z_{photo} to be at least 0.04 smaller/greater than that of their nearby bright galaxies. Here 0.04 is chosen to be about 2σ given the average photo- z error of redMaGiC. Requiring that all foreground and background galaxies having well-defined shape measurements yields 281114 galaxies in total.

Table 1 summarizes the data sets we have defined in Secs. 2.3 and 2.4, with detailed sample size information provided.

2.5 Summary of physical parameters

Similar to our analysis in Paper I, we aim to identify predictors that significantly influence the satellite alignment effect from a large parameter pool. Almost all of the physical pa-

rameters explored in this work are the same as in Paper I, except for one newly added variable: *fracDeV*.

The *cmodel* magnitude systems in SDSS pipeline tries to fit galaxy light profile by taking the linear combination of both de Vaucouleurs and exponential profiles, and stores the coefficient of the de Vaucouleurs term in the quantity *fracDeV*, which describes the fraction of light from a fit to a de Vaucouleurs profile. For a galaxy that can be best fitted by pure exponential profile, *fracDeV* = 0, while *fracDeV* = 1 for pure de Vaucouleurs profile. In general, the brightness distribution of disks follows the exponential profile, whereas bulges are better described with a de Vaucouleurs profile. The *fracDeV* parameter thus can be viewed as a tracer for a galaxy’s angular momentum content or its overall morphology, which has similar but not identical information to galaxy color. It is interesting to check the dependence of angular momentum on SA signal.

In total, we have one response variable (ϕ_{sat}) and 17 other variables constituting the pool of possible predictors for ϕ_{sat} . We classify the 17 parameters into three categories: satellite-related quantities, central galaxy-related quantities and cluster-related quantities. A brief summary of important information about these parameters is in Table 2; we refer readers to Sec. 2.2 of Paper I for details.

3 OVERALL SIGNAL OF SATELLITE ALIGNMENT

3.1 Distribution of ϕ_{sat}

The dark blue filled circles in the left panel of Fig. 2 indicate the p_{mem} -weighted distribution of the SA angle, ϕ_{sat} , for our 174180 satellites in the DR8 footprint, based on the re-Gaussianization shape measurements. The weighted average SA angle is $\langle \phi_{\text{sat}} \rangle = 44.92^\circ \pm 0.07^\circ$, consistent with no net tendency for SA.

However, it does not rule out the possibility of a statistically significant SA detection for subsamples of the satellite population. We will show later in Sec. 4.2 that when focusing on brighter satellites, we can still detect a statistically significant SA signal using re-Gaussianization shapes.

3.2 SA measurement in e_+

Besides using the parameter ϕ_{sat} to quantify the degree of SA signal, it is also useful to calculate the mean radial ellipticity (e_+), especially when quantifying the level of IA systematics to weak lensing signals (e.g., Schneider et al. 2013; Sifón et al. 2015). Here we also compute mean radial ellipticities in order to compare with previous work. For the definition of e_+ , we refer readers back to Sec. 2.2.1 for more detail. Under our definition, a satellite with $e_+ > 0$ tends to point radially toward its host central galaxy.

The dark blue filled circles in Fig. 3 show the averaged (e_+) component based on re-Gaussianization shapes for all DR8 footprint satellites, divided into bins in projected separation from their own central galaxy. The corresponding error bars are simply the standard error of the mean. We observe that the SA signal is consistent with zero within 3σ across all radial bins, meaning that we do not detect any

Table 1. Sample sets used in this work. The upper part of the table shows the two cluster subsamples used for the overall measurement of the satellite alignment effect, as described in Sec. 2.3. The columns indicate the total number of satellites (N_{sat}), total number of distinct clusters (N_{cluster}), and the effective number of central-satellite pairs for each sample after weighting by p_{mem} (N_{eff}). The lower part of the table summarizes the subsamples used for systematic tests, as described in Sec. 2.4. The columns indicate the total number of galaxies (N_{tot}), number of foreground (N_{fore}) and background objects (N_{back}), respectively.

Cluster system sample	N_{sat}	N_{cluster}	N_{eff}
DR8 footprint sample	174180	8121	132072
DR7 footprint sample	158537	7385	120200
Systematic test sample	N_{tot}	N_{fore}	N_{back}
Foreground & background of redMaPPer (DR8 footprint)	45030	4459	40571
Foreground & background of redMaPPer (DR7 footprint)	41075	4134	36941
Non-cluster field sample	697308		
Foreground & background of $m_r < 19$ non-cluster field bright galaxies	278204	6990	271214

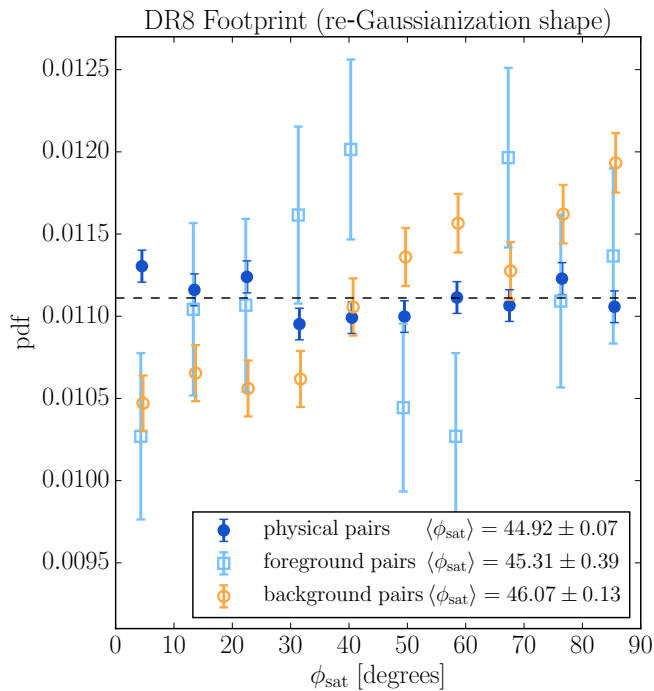


Figure 2. p_{mem} -weighted probability density distribution of SA angle, ϕ_{sat} , for the 174180 $p_{\text{mem}} > 0.55$ pairs measured using the re-Gaussianization method. The dark blue filled circles indicate the pdf of ϕ_{sat} for central-satellite pairs of redMaPPer clusters selected using $p_{\text{mem}} > 0.55$. The weighted averaged SA angle, $\langle\phi_{\text{sat}}\rangle$, is consistent with 45° within error bar, indicating that the overall SA signal measured based on re-Gaussianization shape is not very significant. The open markers show the probability density function (pdf) of ϕ_{sat} for foreground (light blue square) and background (orange circle) pairs in the footprint of redMaPPer clusters. As expected, the $\langle\phi_{\text{sat}}\rangle$ value for foreground is consistent with random, and there is tangential alignment signal $\langle\phi_{\text{sat}}\rangle > 45^\circ$ for backgrounds. The horizontal black dashed line shows the expected result for randomly oriented satellite galaxies.

significant SA effect in the overall redMaPPer satellite population. The grey triangles indicate the measured averaged ellipticity component (e_x), which provides a 45° systematic test (also known as B-mode test). By symmetry, the expected $\langle e_x \rangle$ value should be zero, unaffected by either lensing

or SA effects, which only contribute to the e_+ component. We find that our measured $\langle e_x \rangle$ is consistent with zero in all radial bins, suggesting that systematic errors that would generate a B-mode signal are negligible.

While there is no coherent radial orientation of satellites across the entire DR8 sample, as we will show later in Sec. 4.2, more luminous satellites tend to have stronger SA signal. Here we demonstrate that a subsample of satellites with $^{0.1}Mr < -21$ has $\langle e_+ \rangle \approx 0.014 \pm 0.0042$ ($\sim 3.3\sigma$) and $\langle e_+ \rangle \approx 0.0062 \pm 0.0028$ ($\sim 2.3\sigma$) in the two smallest radial bins at $\sim r < 0.2R_{200m}$, as shown in the red pentagons of Fig. 3. In comparison, Sifón et al. (2015) found no significant SA across all radial bins for satellites with $^{0.1}Mr < -21$ (see their Fig. 10) when using satellites of 91 massive galaxy clusters with shape measurements optimized for lensing. Similarly, Schneider et al. (2013) also found no apparent SA signal across all radial bins for early-type satellites based on members of galaxy groups (see their Fig. 7).

3.3 SA signal based on different shape measurements

To investigate the effect of shape measurement methods on the detection of SA signals, we use satellites within the DR7 footprint, as defined in Sec. 2.3 (see also Table 1), which have re-Gaussianization, deVaucouleurs, and isophotal shape measurements. The left panel of Fig. 4 shows the p_{mem} -weighted distribution of ϕ_{sat} for this sample set, with the teal green circles, yellow green diamonds and olive triangles representing shape measurements based on the re-Gaussianization method, de Vaucouleurs fits, and isophotal fits, respectively. The isophotal shape measurement produces the strongest SA signal ($\langle\phi_{\text{sat}}\rangle = 44.35^\circ \pm 0.08^\circ$), followed by de Vaucouleurs fits ($\langle\phi_{\text{sat}}\rangle = 44.71^\circ \pm 0.08^\circ$) and finally re-Gaussianization shapes ($\langle\phi_{\text{sat}}\rangle = 44.91^\circ \pm 0.08^\circ$). However, as described in Hao et al. (2011), we still must test whether the detected SA signal is real (due to physical alignments) or fake (due to systematics). We will investigate possible systematic effects in Sec. 5.

3.4 Foreground and background systematic tests

We examine our SA measurement using sample sets of foreground and background galaxies in the footprint of redMaPPer cluster field. For construction of foreground and back-

Table 2. A summary of the 17 parameters used to study the satellite alignment effect.

Response Variable	Properties
ϕ_{sat}	<ul style="list-style-type: none"> • Satellite alignment angle, as demonstrated in Fig. 1. • We use this parameter as a response variable to quantify the level of satellite alignment. Smaller ϕ_{sat} indicates a stronger satellite alignment effect.
<hr/>	
Satellite Galaxy Quantities	Properties
$\log(r/R_{200\text{m}})$	<ul style="list-style-type: none"> • Member distance from the cluster central galaxy, normalized by $R_{200\text{m}}$
satellite $^{0.1}M_r$	<ul style="list-style-type: none"> • r-band absolute magnitude of the satellite, k-corrected to $z = 0.1$
satellite $^{0.1}M_g - ^{0.1}M_r$	<ul style="list-style-type: none"> • Color of the satellite galaxy, k-corrected to $z = 0.1$
satellite ellipticity	<ul style="list-style-type: none"> • Satellite ellipticity as defined in Eq. 2
$\Delta\log(\text{satellite } R_{\text{eff}})$	<ul style="list-style-type: none"> • The excess of galaxy size with respect to the predicted size at the same luminosity $\Delta\log(\text{satellite } R_{\text{eff}}) \equiv \text{measured } \log(\text{satellite } R_{\text{eff}}) - \text{predicted } \log(\text{satellite } R_{\text{eff}})$ • The predicted $\log(\text{satellite } R_{\text{eff}}) = -0.20(\text{satellite } ^{0.1}M_r) - 3.84$, derived by linearly fit to all $p_{\text{mem}} > 0.55$ satellites in the DR8 footprint sample. A relevant figure is presented in Fig. 5 of Paper I, except that the derived predicted $\log(\text{satellite } R_{\text{eff}})$ is slightly different from Paper I due to the inclusion of lower p_{mem} satellites in Paper II.
fracDeV	<ul style="list-style-type: none"> • The fractional flux contribution of the de Vaucouleurs profile, see Sec. 2.5 for detail. • $\text{fracDeV} = 0$ for a pure exponential profile; $\text{fracDeV} = 1$ for a pure de Vaucouleurs profile.
θ_{cen}	<ul style="list-style-type: none"> • Central galaxy alignment angle, as demonstrated in Fig. 1 • Smaller θ_{cen} indicates that the satellite is residing closer to the major axis direction of its central galaxy.
<hr/>	
Central Galaxy Quantities	Properties
central galaxy dominance	<ul style="list-style-type: none"> • Magnitude gap between the central galaxy and the mean of the 2nd and 3rd brightest satellites $\text{Central dominance} \equiv \text{Central } ^{0.1}M_r - \frac{^{0.1}M_{r,1\text{st}} + ^{0.1}M_{r,2\text{nd}}}{2}$ • A smaller value indicates a more dominant central galaxy.
central $^{0.1}M_r$	<ul style="list-style-type: none"> • r-band absolute magnitude of the central, k-corrected to $z = 0.1$
central $^{0.1}M_g - ^{0.1}M_r$	<ul style="list-style-type: none"> • Color of the central galaxy, k-corrected to $z = 0.1$
central ellipticity	<ul style="list-style-type: none"> • Ellipticity of central galaxy as defined in Eq. 2.
$\Delta\log(\text{central } R_{\text{eff}})$	<ul style="list-style-type: none"> • The excess of central galaxy size with respect to the predicted size of centrals at the same luminosity. $\Delta\log(\text{central } R_{\text{eff}}) \equiv \text{measured } \log(\text{central } R_{\text{eff}}) - \text{predicted } \log(\text{central } R_{\text{eff}})$ • The predicted $\log(\text{central } R_{\text{eff}}) = -0.31(\text{central } ^{0.1}M_r) - 6.16$, derived by linearly fit to all centrals in the DR8 footprint sample. See also Fig. 4 in Paper I for more detail.
P_{cen}	<ul style="list-style-type: none"> • Central galaxy probability provided in redMaPPer. • P_{cen} is an indicator of whether a cluster system contains only a single dominant central galaxy or has multiple central galaxy candidates.
<hr/>	
Cluster Quantities	Properties
$\log(\text{richness})$	<ul style="list-style-type: none"> • Cluster richness taken from the redMaPPer catalog.
redshift	<ul style="list-style-type: none"> • Cluster redshift estimated by redMaPPer.
cluster ellipticity	<ul style="list-style-type: none"> • Calculated based on the distribution of member galaxies. See Sec. 2.2.3 of Paper I for detail. • A cluster with larger cluster ellipticity has more elongated satellite distribution.
cluster member concentration, Δ_R	<ul style="list-style-type: none"> • Derived based on the average projected distance of member galaxies from the cluster center, with some normalization towards cluster richness and redshift. See Sec. 2.2.9 of Paper I for detail definition. • By construction, negative Δ_R value means the cluster has a more compact member galaxy distribution than the average cluster at similar richness and redshift.

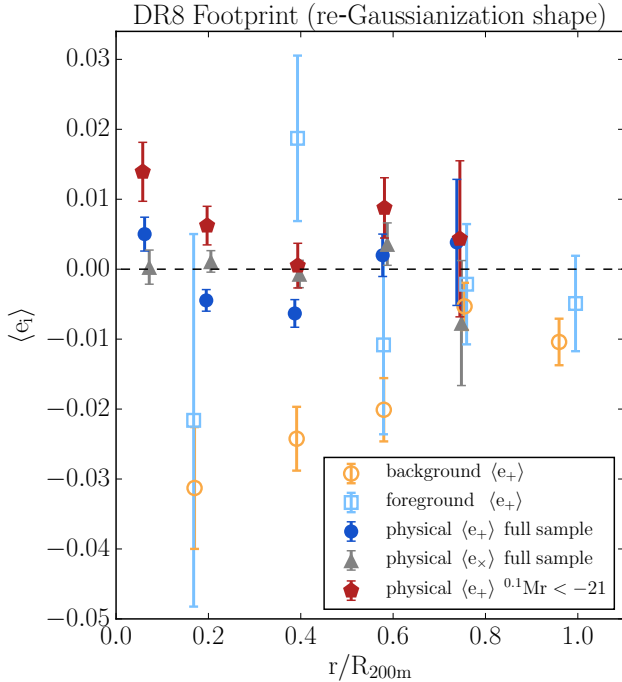


Figure 3. Satellite alignment signal measured in $\langle e_+ \rangle$ (dark blue filled circle) in bins of normalized projected distance based on re-Gaussianization shapes for the 174180 DR8 redMaPPer $p_{\text{mem}} > 0.55$ satellites. Under our definition, $\langle e_+ \rangle > 0$ indicates radial alignment. The measured SA signal is consistent with zero within 3σ across all radial bins. The $\langle e_+ \rangle$ signals for foregrounds (light blue square) and backgrounds (orange open circle) in redMaPPer cluster fields are also shown. The $\langle e_x \rangle$ component for physical pairs, indicated in grey triangles, is consistent with zero in all radial bins. This suggests that systematics that would cause a B-mode signal in the re-Gaussianization shapes are negligible. When focusing on a subsample of brighter satellites with $^{0.1}Mr < 21$ (red pentagon), we find $\langle e_+ \rangle \approx 0.014 \pm 0.0042$ ($\sim 3.3\sigma$) and $\langle e_x \rangle \approx 0.0062 \pm 0.0028$ ($\sim 2.3\sigma$) in the two smallest radial bins at $\sim r < 0.2R_{200m}$. This indicates that we reach a significant SA detection using re-Gaussianization shapes with satellites that are more luminous and located closer to central galaxies.

ground samples, we refer readers back to Sec. 2.4. For foregrounds, we expect galaxies to be randomly oriented in the measured ϕ_{sat} with respect to the central galaxies of redMaPPer clusters in the same field. For backgrounds, we expect galaxies to exhibit tangential alignment because of the gravitational lensing effect. The light blue squares/orange open circles in Fig. 2 show the distribution of ϕ_{sat} measured using re-Gaussianization shapes for our foreground/background samples. The observed ϕ_{sat} distributions are consistent with our expectation. This indicates that there are no severe systematics due to the complexity of measuring shapes in cluster fields based on re-Gaussianization method. However, the test we applied is not very sensitive for low-level systematics due to the lack of foreground pairs.

Besides the test for re-Gaussianization shape, Fig. 5 shows the foreground (light blue square) and background (orange open circle) tests for de Vaucouleurs shape (left panel) and isophotal shape (right panel). For foregrounds, the p -values of KS tests, as indicated in the legend below the

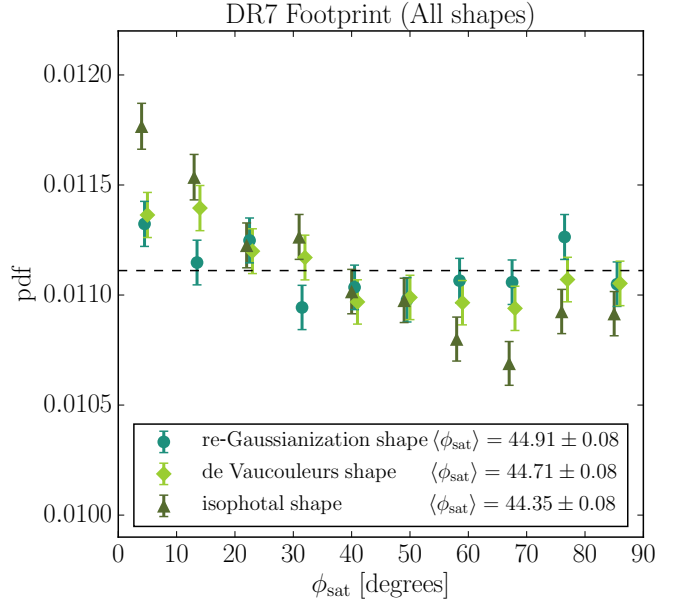


Figure 4. p_{mem} -weighted probability density distribution of ϕ_{sat} for the 158537 $p_{\text{mem}} > 0.55$ redMaPPer satellites in the DR7 footprint based on re-Gaussianization (teal green circle), de Vaucouleurs (yellow green diamond), and isophotal (olive triangle) shape measurements. The weighted average SA angles, $\langle \phi_{\text{sat}} \rangle$, for both de Vaucouleurs and isophotal shapes are less than 45° , indicating we have observed SA effect significantly based on these two shape measurements. However for re-Gaussianization shape, $\langle \phi_{\text{sat}} \rangle$ is consistent with 45° within error bars.

figures, show that the distribution is consistent with uniform distribution. For backgrounds, we also observe the expected lensing effect in de Vaucouleurs and isophotal shaps.

4 LINEAR REGRESSION ANALYSIS

We apply linear regression analysis and variable selection techniques to properly account for correlations among various parameters and to identify featured predictors that significantly affect the SA phenomenon. The variable selection methods are quite similar (but not identical) to those described in Sec. 3 of Paper I. Below, we briefly summarize the approaches, including the new methodology in this paper, and report the results.

4.1 Methodology

4.1.1 Overview of Linear Regression

Linear regression is a method to study the relationship between a response variable Y and a variety of regressors vectorized as $\mathbf{X} = (X_1, X_2, X_3, \dots, X_N)$. One tries to estimate optimal values of the free parameters by minimizing the squared residuals of the following model:

$$Y = f(\mathbf{X}) = \beta_0 + \beta_1 X_1 + \dots + \beta_i X_i + \dots + \beta_N X_N + \epsilon, \quad (4)$$

where the intercept β_0 and the slopes β_i are the unknown regression coefficients, and ϵ represents random observational

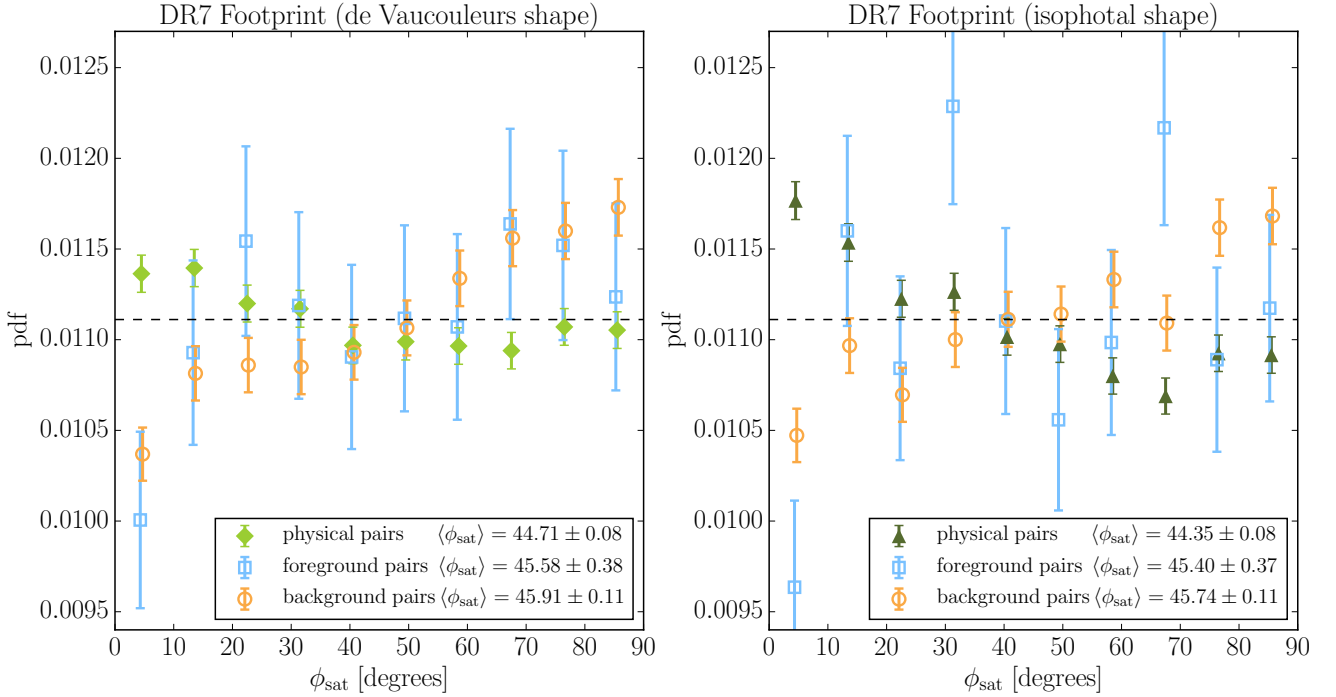


Figure 5. Foreground (light blue open square) and background (orange open circle) tests for de Vaucouleurs (left panel) and isophotal shape (right panel) measurements.

error, usually assumed to be distributed normally with mean zero and some dispersion.

In our analysis, we use ϕ_{sat} as the response variable Y , regressed against the 17 parameters in our parameter pool, as listed in Table 2. In short, we have 7 satellite-related, 6 central galaxy-related and 4 cluster-related quantities. When fitting the regression Eq. (4), we standardize the parameters P_i :

$$X_i = \frac{P_i - \langle P \rangle_i}{\sigma_{P_i}}, \quad (5)$$

where $\langle P \rangle_i$ and σ_{P_i} are the sample mean and standard deviation respectively of the parameter P_i , with the latter representing the width of the intrinsic scatter combined with measurement error. Table 3 lists the $\langle P \rangle$ and σ_P for our 17 parameters for DR8 redMaPPer satellites. The standardization means that even though our predictors P_i have different magnitudes and spreads, the fitted values β_i all have essentially the same meaning: larger $|\beta_i|$ indicates a stronger effect of the regressor X_i on ϕ_{sat} . We also quantify the level of significance for any identified correlations using the t -value. The t -value, defined as the ratio of β_i to its standard error, can be positive or negative depending on the sign of β_i . A larger $|t|$ indicates a higher likelihood that $\beta_i \neq 0$, which means a stronger relationship between ϕ_{sat} and X_i . Statistically, under the assumption that β_i is asymptotically normal,³ there

³ Suppose we do many measurements on β_i , with different but statistically similar sets of data, and plot the distribution of the resulting β_i . We say β_i is asymptotically normal if the distribution is a gaussian at the mean of the true β_i value with certain variance.

is a direct link between the t -value and p -value on the hypothesis test of whether $\beta_i = 0$ or not. A p -value of 0.05 corresponds to a 95% confidence interval for β_i that does not overlap with zero. We will count predictors with p -value < 0.05 as having significant effect on SA signal when doing model selection later.

4.1.2 Model Averaging

The next issue we need to face is how to choose a model with predictors that truly affect ϕ_{sat} . A linear model with all possible predictors has many free parameters to tune to fit the data well, but may cause high variance. By contrast, a model with only few predictors is more stable, but may underfit the data yielding a high bias. A good model results from achieving a balance between goodness of fit and complexity. With 17 predictor candidates in our parameter pool, there are a total of 2^{17} ($= 131\,072$) possible models.

In Paper I, we applied standard ‘‘Forward Stepwise’’ and ‘‘Best Subset’’ model selection methods to identify a single best model, and interpreted our results based on that model alone. However, SA is a relatively weak signal, so identifying predictors that reflect the true underlying physics rather than noise requires a careful treatment of model uncertainty, which can lead to the selection of a model that by random chance includes uninformative predictors. Thus in this work, we apply the ‘‘model averaging’’ technique (see e.g. Burnham & Anderson 2003 and Grueber et al. 2011, and references therein), which combines a portion of ‘good models’ from the parent model pool by taking a weighted-average based on the performance scores of each model measured by some information criterion (such as AIC; Akaike 1998). Through

the model averaging process, fluctuations due to noise can be averaged out and the combined model is thus more stable.

The detailed model averaging analysis proceeds as follows:

(i) As was the case in Paper I, we use best-subset selection to fit each of the 2^{17} possible models using R's `leaps` package, and for each we estimate the AIC:

$$AIC_i = \frac{1}{n\hat{\sigma}_i^2}(RSS_i + 2d_i\hat{\sigma}_i^2), \quad (6)$$

where RSS_i is the residual sum of squares, d_i is the number of predictors used in the i^{th} model, $\hat{\sigma}_i^2$ is an estimate of the variance of observational error ϵ shown in Eq. (4), and n is the total number of satellite-central pairs. A lower AIC value indicates a better-fitting model.

(ii) We convert each AIC value to a relative quantity:

$$\Delta AIC_i = AIC_i - \min(AIC), \quad (7)$$

where $\min(AIC)$ represents the smallest AIC value of all possible models in the previous step.

(iii) Given the set of relative AIC values, we compute the model-averaging weight for each model:

$$w_i = \frac{\exp(-\Delta AIC_i/2)}{\sum_{k=1}^{2^{17}} \exp(-\Delta AIC_k/2)}. \quad (8)$$

(iv) For computational efficiency, we apply a cut of $\Delta AIC = 12$, meaning that we only average that subset of 485 models with $\Delta AIC_i < 12$. For this cut, the sum of weights is 0.996.

(v) The final averaged regression estimate $\tilde{\beta}_j$ and variance estimate $\tilde{\sigma}_j^2$ for each of the 17 predictors are given by

$$\tilde{\beta}_j = \sum_i w_i \beta_{j,i} \mathbf{I}(\beta_j \in \mathcal{M}_i) \quad (9)$$

$$\tilde{\sigma}_j^2 = \sum_i w_i [\sigma_{j,i}^2 + (\beta_{j,i} - \tilde{\beta}_j)^2] \mathbf{I}(\beta_j \in \mathcal{M}_i). \quad (10)$$

The first summation can be read as “taking weighted average of the of the j^{th} regression coefficient over all models with $\Delta AIC_i < 12$ where the j^{th} regressor appears” (as indicated by the indicator function \mathbf{I}). The second summation is the variance of the j^{th} regressor. If the estimated $\tilde{\beta}_j$ is more than $1.96 \tilde{\sigma}_j$ away from zero, assuming $\tilde{\beta}_j$ is distributed normally with mean zero, this corresponds to a p value < 0.05 that $\tilde{\beta}_j \neq 0$. One can interpret that the predictor j is important for the SA signal.

We note that the way in which $\tilde{\beta}_j$ is computed has the effect of shrinkage: the smaller number of models in which $\tilde{\beta}_j$ appears, the closer $\tilde{\beta}_j$ gets to zero. This method for computing $\tilde{\beta}_j$ is dubbed the zero method (Burnham & Anderson 2003), which is contrasted against the natural average method, where we normalize the predictor estimate by dividing by $\sum_i w_i \mathbf{I}(\beta_j \in \mathcal{M}_i)$. The zero method is preferable in situations such as ours where the aim is to determine which predictors have the strongest effects on the response variable.

4.2 Featured Predictor Selection – re-Gaussianization shape

In this subsection, we report the predictor selection result for our DR8 footprint sample with ϕ_{sat} measured using the re-Gaussianization method. All analyses below are properly weighted by p_{mem} for each satellite-central pair.

Table 4 lists those models that have $\Delta AIC < 3$, with the first row containing the model with the smallest AIC value, i.e., the model that would be selected in a traditional implementation of best-subset selection using AIC as the fit metric (or equivalently using Mallows's C_p , which is proportional to AIC). The first column indicates the total number of regressors included in a model, and the subsequent 2nd to the 18th columns records the regression coefficients β_j formulated in Eq. (4). Some predictors, such as $\log(r/R_{200\text{m}})$ and satellite luminosity $^{0.1}Mr$, appear in all of the top models, while less important predictors appear only occasionally. In Table 5 we list the values of $\tilde{\beta}$ and $\tilde{\sigma}$, as well as the absolute t value, for each predictor after averaging over all models with $\Delta AIC < 12$ (485 models in total; see eqs. (9) and (10)). Predictors with $|t| > 1.96$ are identified as significant in affecting SA. Under the re-Gaussianization shape measurement, we identify $\log(r/R_{200\text{m}})$, $^{0.1}Mr$, satellite ellipticity e_{sat} , and $fracDev$ as significant predictors. To reiterate a point made above, in this work we are not interested in using the $\tilde{\beta}$ values to predict ϕ_{sat} ; our interest lies in quantifying the significances of the predictors (as indicated by t values) and in exhibiting their effect on ϕ_{sat} (as indicated in the sign of $\tilde{\beta}$).

Fig. 6 illustrates these trends by plotting the averaged value of ϕ_{sat} in bins of each selected featured predictor, with the correlation coefficient between ϕ_{sat} and each predictor also provided. Clearly the satellite luminosity ($^{0.1}Mr$) and separation from the central galaxy in units of $R_{200\text{m}}$ ($\log(r/R_{200\text{m}})$) are prominent predictors for satellite alignments. There are sub-populations with measured $\langle \phi_{\text{sat}} \rangle > 45^\circ$, although with less than 3σ significance, for example at faint luminosity or low $fracDev$. This may in part be due to lensing contamination from background galaxies that are wrongly included in the satellite sample. The orange triangular points shown in Fig. 6 are the estimates of lensing contamination based on the assumption that the p_{mem} values accurately reflect reality; we refer readers to Appendix B for details. The estimated contribution from lensing contamination to $\langle \phi_{\text{sat}} \rangle \approx 45.1^\circ$ across all subsamples.

In Sec. 3.1 and 3.2, no SA signal was detected based on re-Gaussianization shape measurement, when averaging over all satellite-central pairs. The results in this section demonstrate that there do exist statistically significant SA effects for certain subsamples of satellites, such as those that are intrinsically brighter or located closer to their host central galaxies. We further discuss these selected predictors in Sec. 6.

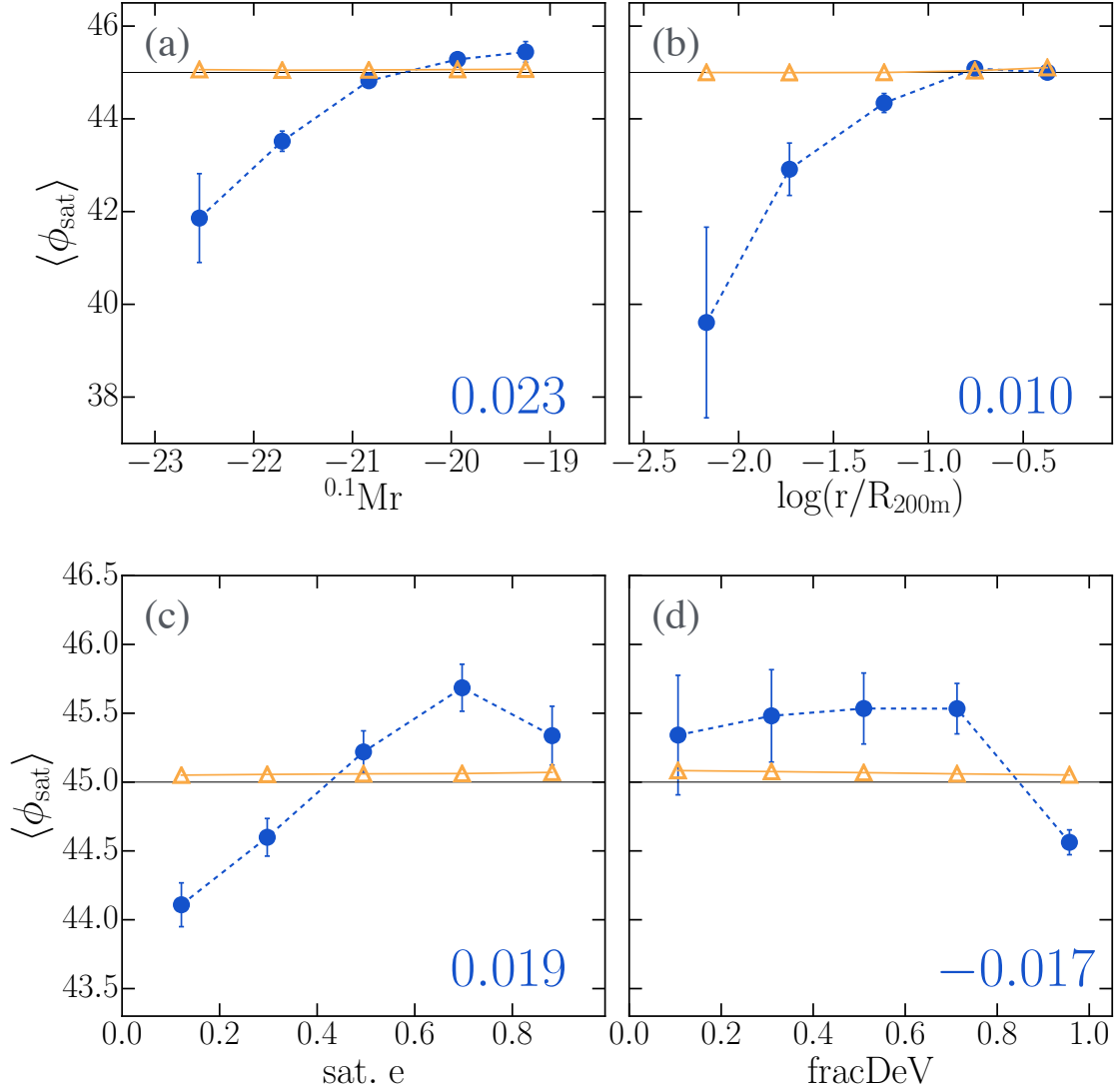


Figure 6. Averaged satellite alignment angle $\langle \phi_{\text{sat}} \rangle$ of redMaPPer member galaxies in the SDSS DR8 footprint sample as a function of the 4 significant predictors whose $|t| > 1.96$ shown in Table 5. The correlation coefficient between ϕ_{sat} and each predictor is labeled on the lower-right corner of each panel. One can see that $\langle \phi_{\text{sat}} \rangle < 45^\circ$ for satellites that have higher luminosity, are located closer to cluster center, are rounder in shape, and have a higher *fracDeV*. Especially for the subsamples of luminous satellites, we detect a very significant SA signal. The triangular orange markers show the estimated level of lensing contamination from background galaxies that are wrongly included in the SA analysis (see Appendix B for details), resulting in $\langle \phi_{\text{sat}} \rangle \sim 45.1^\circ$ across all bins.

Table 3. Mean and standard deviation values (weighted by p_{mem}) of the 17 parameters for our DR8 $p_{\text{mem}} > 0.55$ redMaPPer satellites.

	$\log(r/R_{200m})$	$0.1 Mr$	color	e_{sat}	$R_{\text{eff,sat}}$	θ_{cen}	fDeV	dom	$0.1 Mr_{\text{cen}}$	color _{cen}	e_{cen}	$R_{\text{eff,cen}}$	P_{cen}	λ	z	e_{cluster}	ΔR
mean	-0.68	-20.40	0.89	0.45	1.32	42.09	0.77	-0.89	-22.35	0.98	0.25	0.02	0.87	41.99	0.24	0.20	0.01
std.	0.34	0.76	0.12	0.26	0.20	26.09	0.30	0.60	0.49	0.07	0.16	0.15	0.17	25.01	0.07	0.11	0.11

Table 4. A subset of top regression models ranked by the goodness of performance for DR8 re-Gaussianization shape measurements. The 1st column is the total number of predictors involved in a model, columns 2 ~ 18 show the regression coefficients for our 17 predictors listed in the same order as that of Table 2. The 2nd last column lists the ΔAIC values, and the last column shows the weighting factor for each model that we applied when doing model averaging.

Np	$\log(r/R_{200m})$	$0.1 Mr$	color	e_{sat}	$R_{\text{eff,sat}}$	θ_{cen}	fDeV	dom	$0.1 Mr_{\text{cen}}$	color _{cen}	e_{cen}	$R_{\text{eff,cen}}$	P_{cen}	λ	z	e_{cluster}	ΔR	ΔAIC	weight
6	0.32	0.49		0.28	-0.14		-0.28		-0.16									0	0.0296
7	0.32	0.49		0.28	-0.14	0.08	-0.28		-0.16									0.82	0.0196
7	0.32	0.48		0.29	-0.14	-0.28	-0.28		-0.16			0.06						1.49	0.014
7	0.31	0.47		0.29	-0.14	-0.3	-0.3		-0.17					-0.06				1.52	0.0138
7	0.32	0.49		0.28	-0.14	-0.28	-0.28		-0.16		0.05							1.64	0.013
7	0.32	0.49		0.28	-0.14	-0.28	-0.28	-0.05	-0.13									1.81	0.012
7	0.32	0.49		0.28	-0.14	-0.28	-0.28		-0.17	-0.04								1.83	0.0118
5	0.31	0.5		0.32		-0.23	-0.23		-0.17									1.9	0.0115
6	0.32	0.48		0.28	-0.14	-0.28	-0.28	-0.14										2.01	0.0108
7	0.32	0.49		0.28	-0.14	-0.28	-0.28		-0.16									2.15	0.0101
7	0.32	0.49	-0.02	0.28	-0.14	-0.27	-0.27		-0.16							-0.02		2.22	0.0098
7	0.32	0.49		0.28	-0.14	-0.28	-0.28		-0.16									2.24	0.0097
8	0.32	0.48		0.28	-0.14	0.08	-0.28		-0.16			0.06						2.25	0.0096
7	0.32	0.49		0.28	-0.14	-0.28	-0.28		-0.16				0.01					2.26	0.0096
7	0.32	0.49		0.28	-0.14	-0.28	-0.28		-0.16					0				2.27	0.0095
8	0.31	0.47		0.29	-0.14	0.08	-0.29		-0.17						-0.06			2.31	0.0093
8	0.32	0.49		0.28	-0.14	0.08	-0.28		-0.16		0.05							2.44	0.0087
8	0.32	0.49		0.28	-0.14	0.08	-0.28	-0.06	-0.13									2.61	0.008
8	0.32	0.49		0.28	-0.14	0.07	-0.27		-0.17	-0.04								2.67	0.0078
7	0.32	0.48		0.28	-0.14	-0.28	-0.28	-0.15						0.08				2.68	0.0078
6	0.31	0.5		0.31		0.07	-0.23		-0.17									2.76	0.0075
7	0.32	0.48		0.28	-0.14	0.08	-0.28	-0.14										2.83	0.0072

Table 5. Model averaged result for our DR8 footprint sample (see Table 1) based on re-Gaussianization shape measurements. The 1st row shows the estimated regression coefficient based on Eq. (9). The 2nd row lists the standard error of $\hat{\beta}$. The 3rd row is the absolute value of the t value = $|\hat{\beta}/\hat{\sigma}|$. Parameters with $|t| > 1.96$ is identified as important predictors in affecting SA effect. Here we find that $\log(r/R_{200m})$, $^{0.1}\text{Mr}$, satellite ellipticity, and fracDeV are selected as significant predictors.

	$\log(r/R_{200m})$	$^{0.1}\text{Mr}$	color	e_{sat}	$R_{\text{eff,sat}}$	θ_{cen}	fDeV	dom	$^{0.1}\text{Mr}_{\text{cen}}$	color _{cen}	e_{cen}	$R_{\text{eff,cen}}$	P_{cen}	λ	z	e_{cluster}	ΔR
$\hat{\beta}$	0.314	0.48	-0.003	0.289	-0.115	0.032	-0.273	-0.028	-0.133	-0.008	0.011	0.012	0.001	0.005	-0.016	-0.003	0.001
$\hat{\sigma}$	0.063	0.07	0.026	0.068	0.065	0.049	0.074	0.059	0.069	0.032	0.035	0.035	0.023	0.03	0.043	0.024	0.02
$ t $	4.982	6.892	0.111	4.257	1.781	0.639	3.71	0.469	1.932	0.258	0.317	0.325	0.037	0.152	0.377	0.123	0.052

Table 6. Model averaged result for our DR7 footprint sample (see Table 1) based on de Vaucouleurs shape measurements. The selected significant predictors ($|t| > 1.96$) are: $\log(r/R_{200m})$, $^{0.1}\text{Mr}$, satellite ellipticity, θ_{cen} , and fracDeV .

	$\log(r/R_{200m})$	$^{0.1}\text{Mr}$	color	e_{sat}	$R_{\text{eff,sat}}$	θ_{cen}	fDeV	dom	$^{0.1}\text{Mr}_{\text{cen}}$	color _{cen}	e_{cen}	$R_{\text{eff,cen}}$	P_{cen}	λ	z	e_{cluster}	ΔR
$\hat{\beta}$	0.628	0.617	-0.021	0.41	-0.02	0.229	-0.218	-0.01	-0.094	-0.035	0.016	0.024	0.046	0.065	0.001	0	-0.003
$\hat{\sigma}$	0.066	0.072	0.046	0.07	0.046	0.065	0.073	0.044	0.074	0.054	0.041	0.048	0.062	0.067	0.021	0.016	0.022
$ t $	9.536	8.62	0.448	5.886	0.433	3.506	2.977	0.227	1.268	0.657	0.397	0.497	0.742	0.979	0.069	0.002	0.133

Table 7. Similar to Table 6 but for results based on isophotal shape measurements. The selected significant predictors ($|t| > 1.96$) are: $\log(r/R_{200m})$, $^{0.1}\text{Mr}$, satellite ellipticity, θ_{cen} , fracDeV , and redshift.

	$\log(r/R_{200m})$	$^{0.1}\text{Mr}$	color	e_{sat}	$R_{\text{eff,sat}}$	θ_{cen}	fDeV	dom	$^{0.1}\text{Mr}_{\text{cen}}$	color _{cen}	e_{cen}	$R_{\text{eff,cen}}$	P_{cen}	λ	z	e_{cluster}	ΔR
$\hat{\beta}$	0.953	0.713	-0.154	0.451	0.003	0.371	-0.325	0.014	-0.022	0.002	0.003	0.001	0.107	0.055	0.177	-0.052	-0.008
$\hat{\sigma}$	0.067	0.079	0.071	0.069	0.03	0.066	0.076	0.051	0.056	0.028	0.028	0.028	0.068	0.062	0.076	0.06	0.033
$ t $	14.282	9.074	2.163	6.498	0.093	5.629	4.301	0.279	0.397	0.063	0.105	0.03	1.57	0.895	2.32	0.868	0.239

4.3 Featured Predictor Selection – de Vaucouleurs and isophotal shapes

Here we repeat the predictor selection process as in the previous section, now using the DR7 sample satellites that have ϕ_{sat} well-measured using all three shape measurement methods. Using both de Vaucouleurs and isophotal shapes result in a nonzero net SA signal detection in the overall sample as shown in Sec. 3.3. It is therefore interesting to check if the predictor selection result is consistent with that based on re-Gaussianization shape, where the detected SA signal is small. If we select a different set of predictors, we must consider whether they are caused by a fake systematic alignment signal captured in de Vaucouleurs and isophotal shapes, or they could be physically reasonable predictors that are authentically associated with the SA phenomenon, but are not selected out in the re-Gaussianization shape due to its sensitivity to different regions of the galaxy light profiles.

We summarize our predictor selection results for de Vaucouleurs and isophotal shapes in Tables 6 and 7. Under the criterion of $|t| > 1.96$, for de Vaucouleurs shape, in addition to the predictors that have been identified based on re-Gaussianization shape (Table 5), one extra predictor, θ_{cen} , is added with a fairly high t -value. For isophotal shape, we identify two new predictors compared to those from re-Gaussianization shapes: θ_{cen} and redshift. As revealed in the sign of the $\tilde{\beta}$, satellites with smaller θ_{cen} (stronger central galaxy alignment with the shape of the satellite galaxy distribution) and smaller redshift have stronger isophotal SA signal.

Fig. 7 shows the averaged SA angle $\langle\phi_{\text{sat}}\rangle$ of our DR7 footprint sample in bins of the identified predictors. The correlation coefficients measured between ϕ_{sat} using the three shape measurements and each predictor are shown in the legend. The correlations become tighter as we move from re-Gaussianization to isophotal shapes for most predictors – $\log(r/R_{200\text{m}})$, satellite $^{0.1}Mr$, satellite ellipticity, θ_{cen} , and fracDev . However, the correlation coefficient for the redshift has a different sign when measured in isophotal shape vs. the other two shapes. We will discuss the redshift dependence in more detail in Sec. 6.

In general, for all differences between methods, we must consider whether they originate from systematic effects, or from real differences between the methods due to their sensitivity to different parts of the galaxy light profiles and isophotal twisting.

5 ORIGIN OF DISCREPANCY IN DETECTED SATELLITE ALIGNMENT SIGNAL WITH DIFFERENT SHAPE MEASUREMENT METHODS

As reported in Fig. 4, the detected SA signal strength depends on shape measurement methods. The isophotal shape detects the strongest SA signal, followed by de Vaucouleurs shape then re-Gaussianization shape. This trend is consistent with the large-scale IA measurement done by Singh & Mandelbaum (2016) using these three shape measurement algorithms.

In this section, we discuss possible reasons for this discrepancy. We note that in cluster systems, the difference in

SA angle ($|\phi_{\text{sat,iso}} - \phi_{\text{sat,reg}}|$) is identical to the PA difference, $|\text{PA}_{\text{iso}} - \text{PA}_{\text{reg}}|$ measured in the RA-dec frame. We can therefore use $|\text{PA}_{\text{iso}} - \text{PA}_{\text{reg}}|$ for our tests, which allows us to introduce galaxies that do not belong to any cluster for tests of statistical and systematic errors.

In what follows, we classify the origin of the discrepancy in the measured galaxy PA into three dominant factors, as summarized in Fig. 8. Our high-level goal is to consider all possible factors that may contribute to the measured difference in average SA angle for our redMaPPer cluster sample, and determine whether the result is dominated by noises and systematics, or we do detect any interesting physical effects.

5.1 PA discrepancies due to noise

The first factor that affects the difference in PA is simply noise. We further separate the origin of noise into ellipticity noise and pixel noise.

5.1.1 Ellipticity noise

The ellipticity noise is perhaps the most dominant factor in determining how precisely the PAs are measured. For a given S/N ratio of a detection, the uncertainty in the PA is larger for rounder galaxy (see Table 1 of Refregier et al. 2012). We demonstrate this effect in Fig. 9a using our non-cluster field sample, as defined in Sec. 2.4. We plot the PA differences between isophotal and re-Gaussianization shapes as a function of the ellipticity based on re-Gaussianization measurement. The filled circle shows the mean of the $|\text{PA}_{\text{iso}} - \text{PA}_{\text{reg}}|$ value in ellipticity bins, revealing that the averaged differences in PA become larger when galaxies are rounder.

5.1.2 Pixel noise

Pixel noise arises from the Poisson noise in the sky and object flux in CCD measurements. Its impact is strongest on the images of faint galaxies, which have relatively low signal but still experience all the Poisson noise due to the background level. Pixel noise makes it difficult to measure the shape of low S/N galaxies, especially when those galaxies are also poorly resolved compared to the PSF (e.g., Refregier et al. 2012). As a consequence, there may also be an apparent redshift trend.

Figs. 9b, 9c, and 9d show the scatter plots for $|\text{PA}_{\text{iso}} - \text{PA}_{\text{reg}}|$ as a function of apparent r -band magnitude, r -band resolution factor⁴, and photo- z respectively from the non-cluster field sample. We can see that the averaged differences in PA (filled circle) go up for galaxies with fainter m_r , lower resolution, and higher z as expected.

5.2 PA discrepancies due to systematic errors

Systematic errors due to data analysis methods or contamination from nearby objects (see Fig. 8) may also cause PA discrepancies between different methods.

⁴ The resolution factor reflects how resolved a galaxy is compared to its PSF, with 0 (1) indicating a completely unresolved (perfectly well-resolved) galaxy. See Appendix A of Reyes et al. (2012) for its definition.

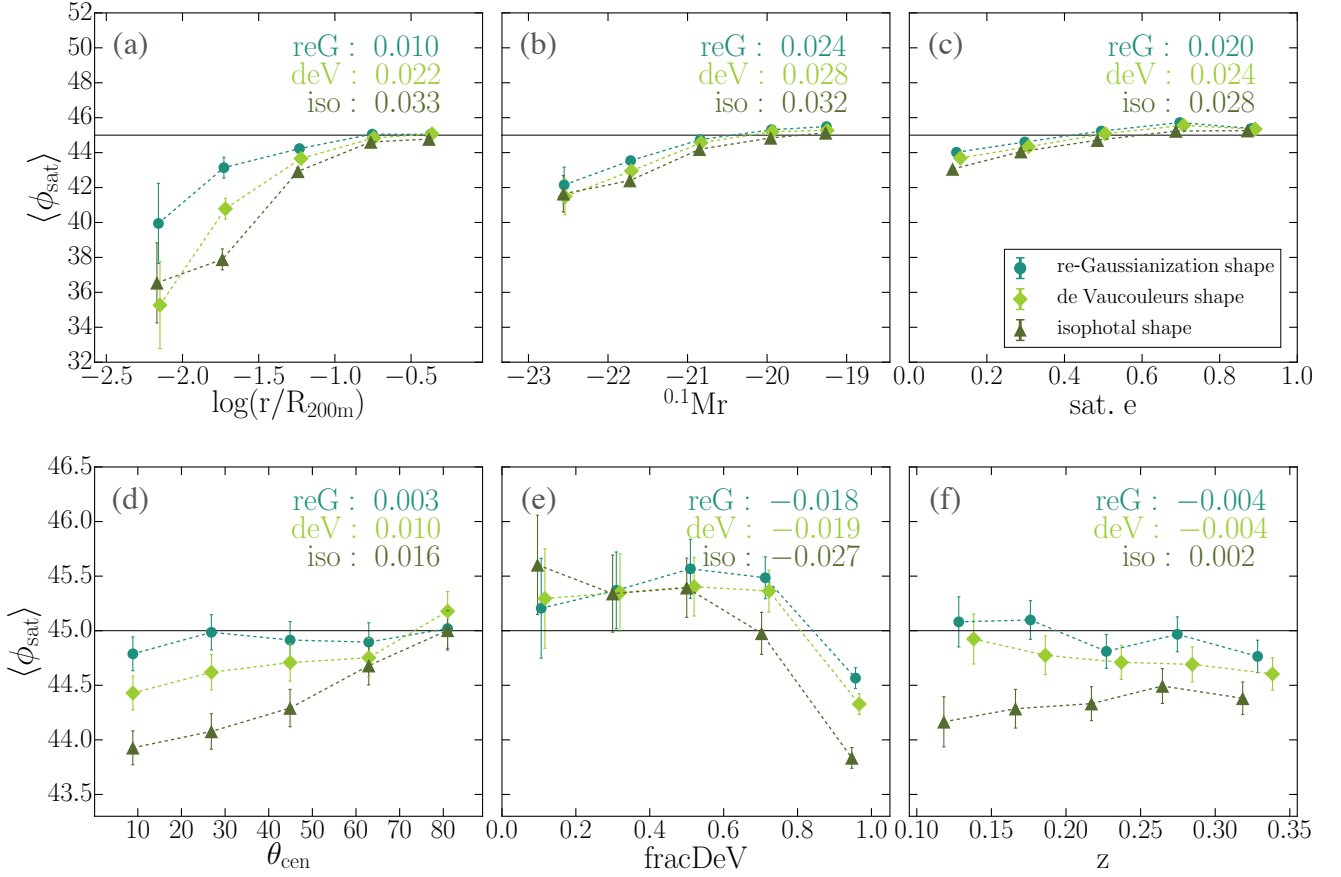


Figure 7. Averaged satellite alignment angle $\langle \phi_{\text{sat}} \rangle$ of redMaPPer members in the SDSS DR7 footprint as a function of the 6 significant predictors whose $|t| > 1.96$ as shown in Tables 6 and 7. Correlation coefficients between ϕ_{sat} and x -axes parameters are shown in the upper right corner of each panel.

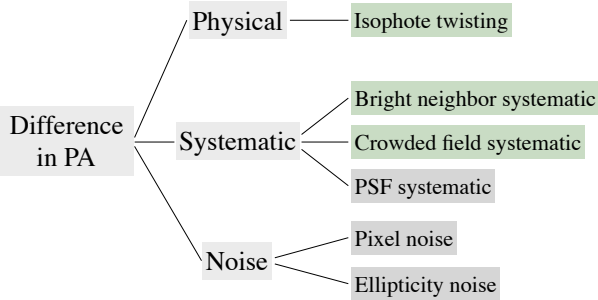


Figure 8. The origin of discrepancies in PA differences measured with different shape measurement methods. Three origins for these discrepancies are explored: discrepancies due real physical isophote twisting effect (Sec. 5.3), discrepancies caused by systematic errors, and discrepancies due to noise. The systematic origins can be further classified into three factors: the bright neighbor and crowded field systematics (Sec. 5.2.2) and the PSF systematic (Sec. 5.2.1). The origins of noise are separated into two sources: pixel (Sec. 5.1.2) and ellipticity noises (Sec. 5.1.1). The items colored in green background are factors that especially important for galaxies residing in cluster fields, while the ones colored in grey background are relevant in all possible environments.

5.2.1 PSF systematics

Different shape measurements correct for the effects of the PSF on galaxy images at different levels. If not removed properly, the residuals of PSF would bias the resulting shape parameters: In the case that PSFs are round and galaxies have elliptical isophotes, on average, the PA will be unaffected by the PSF convolution, with only the magnitude of the galaxy shape being affected. If PSFs are elongated toward specific directions, then both the measured ellipticity and PA of galaxies are contaminated.

Isophotal shapes do not explicitly correct for the PSF convolution; de Vaucouleurs shapes partially correct for the PSF using an approximate (double-Gaussian) PSF model. The re-Gaussianization shapes consider a full PSF model to remove PSF systematics in order to recover small weak lensing signals. Therefore, part of the discrepancy in PA measured based on different shape measurements may be due to different levels of PSF anisotropy removal.

Singh & Mandelbaum (2016) explored the additive bias in galaxy shape measurements due to residual PSF anisotropy, resulting in a coherent additive bias in the measured shapes of SDSS LOWZ galaxies using these three shape measurements. They found that for both re-Gaussianization and isophotal shapes, their additive biases are quite small. However, for de Vaucouleurs shapes, the ad-

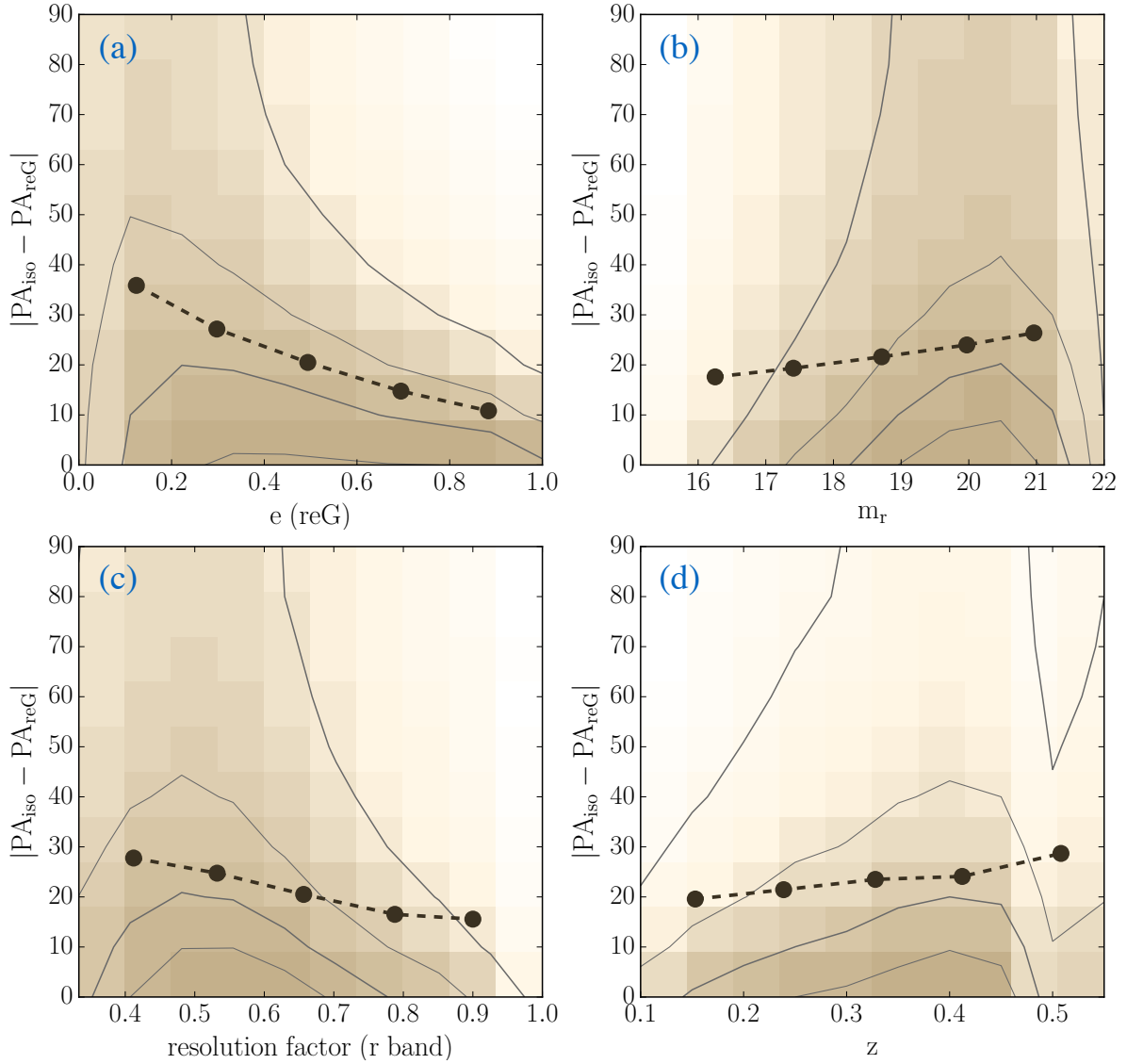


Figure 9. Absolute PA differences between isophotal and re-Gaussianization shapes as a function of galaxy ellipticity, mag r , r-band resolution factor, and redshift. The grey contour levels indicate the level below which 20%, 45%, 70%, and 95% of the central-satellite pairs are located. The filled solid dots indicate the averaged $|PA_{\text{iso}} - PA_{\text{reG}}|$ values in bins of the horizontal axes values. As shown, the averaged differences in PA increase for galaxies that are rounder in shape, with fainter m_r , lower resolution, and located at higher z .

ditive bias is about a factor of 10 larger than with the other two shape measurements (see their Fig. 5). They claimed that this may be due to the fact that the de Vaucouleurs modeling uses an approximate PSF model. If those results are relevant for galaxies in cluster fields, then part of the PA discrepancy between de Vaucouleurs shape and the other two is contributed by the residual PSF anisotropy in the galaxy shapes. In fact, they should be even more important here, because the galaxies used in our analysis are smaller and fainter, resulting in a greater susceptibility to PSF anisotropy modeling errors.

5.2.2 Bright neighbor and crowded field systematics

Different shape measurement methods determine galaxy PA based on different parts of the galaxy's light profile. The re-

Gaussianization method puts more emphasis on the central region of a galaxy's profile. The de Vaucouleurs shape includes both central and outer extended wings of the light profile to fit PA, while the isophotal shape traces the outermost region of a galaxy along the 25 mag/arcsec^2 isophote. These choices may make the latter two methods more sensitive to artifacts in the de-blending and sky subtraction processes, leading to spurious SA signals. The two dominant systematics that affect the de-blending and sky subtraction processes and further contribute to the PA discrepancy are bright neighbor and crowded field systematics. The bright neighbor systematic arises due to the contamination of light from nearby bright neighbors in the galaxy for which we are attempting to measure a shape. In cluster-like high density regions, the measured galaxy PA could be biased coherently pointing toward the high-density direction due to the intr-

acluster light or due to the fact that the large number of bright galaxies causes a misestimated sky gradient. We refer this second effect as the crowded field systematic.

Below we start by estimating the level of bright neighbor systematic. In the left panel of Fig. 10, we show the measured mean absolute PA discrepancy (hereafter, MAPAD) between isophotal and re-Gaussianization shapes as a function of projected sky separation for galaxies that have a bright $m_r < 19$ non-physically associated neighbor, as defined in (iii) of Sec. 2.4 (plotted in purple open points). We see that the MAPAD increases to $\sim 27^\circ$ for the innermost sky separation bin, indicating potentially more contamination from bright neighbors at closer sky separation.

Besides systematics, there is also a noise contribution (see Sec. 5.1) to the measured MAPAD, which must be estimated in order to properly constrain the level of bright neighbor and crowded field systematics. Note that for the MAPAD data points shown in purple open circles in Fig. 10, there is no contribution from a physical effect like isophotal twisting, due to our use of foreground/background galaxies at different redshifts from the bright central galaxies.

To distinguish between bright neighbor systematic and noise, we re-weight the galaxies in our non-cluster field sample (as defined in Sec. 2.4, (ii)) to match the distributions of m_r , z , and ellipticity in the sample around bright galaxies used here. This reweighting is done separately within each bin in projected sky separation. We can then record the weighting factors in the m_r - z -ellipticity space, and use these weighting factors to calculate the weighted-MAPAD from galaxies in the non-cluster field sample. The resulting weighted-MAPAD value is then a proper estimation of the noise level for galaxies in each sky separation bin, assuming that those three quantities are the main ones determining the statistical uncertainty in the MAPAD. The triangular data points in both panels of Fig. 10 show the resulting estimation of the noise level. The convergence of the triangular points towards the circular points at larger separations appears to validate the assumption behind this method.

After subtracting the noise contribution in the left panel of Fig. 10, the remaining signal shown in Fig. 11 (purple open circles) should be dominated by MAPAD due to bright neighborhood systematics. This figure shows that for large sky separations ($\gtrsim 0.4'$), the detected MAPAD is consistent with our prediction for the noise. For the innermost bin in sky separation, the excess of MAPAD, $\Delta \langle |PA_{\text{iso}} - PA_{\text{reG}}| \rangle$, increases to $\sim 7^\circ$ for galaxies that have a bright ($m_r < 19$) neighbor. The best-fitting models of the form

$$\Delta \langle |PA_{\text{iso/deV}} - PA_{\text{reG}}| \rangle = A (\text{sky separation})^B \quad (11)$$

are provided in the legend of Fig. 11, and will later be used to estimate the level of MAPAD due to bright neighbor systematics. The right panel of Fig. 11 shows the same results as in the left panel, but for de Vaucouleurs (rather than isophotal) vs. re-Gaussianization shapes. The trends in both panels are similar.

Aside from the simple diagnostics shown here, Mandelbaum et al. (2005) and Aihara et al. (2011) have also pointed out other ways that the imperfect deblending and sky-subtraction can affect the measured properties of the faint galaxy populations around bright galaxies in SDSS DR4 and DR8 photometry pipelines. We conclude that bright neighbor systematic does play some role in the measured MAPAD

between different shape measurement methods in the data, and its effect increases for galaxies around brighter neighbors.

We attempt to measure the strength of the crowded field systematic by measuring the MAPADs for foreground and background galaxies of redMaPPer clusters as defined in sample (i) of Sec. 2.4. The right panel of Fig. 10 shows the resulting estimate, with the estimated noise contribution shown as well. The difference between the two sets of data points, as shown in the blue filled circles in Fig. 11, indicates the joint contribution of MAPAD due to both bright neighborhood and crowded field systematics in the redMaPPer cluster field. Unfortunately here we lack pairs at small projected sky separation, resulting in a very noisy estimate of these combined effects.

5.3 PA discrepancies due to physical effects

Finally, in the case that a pair of galaxies are physically associated, aside from noise and systematics, some portion of the measured MAPAD could be explained by a real physical effect known as “isophote twisting” (di Tullio 1978; Kormendy 1982). The origin of this phenomenon is that the galaxy outer light profile may be more sensitive to external tidal fields, and hence could show a stronger SA signal compared with its inner light profile.

From N -body simulations, at one halo length scale, Pereira & Bryan (2010) detected a significant amount of isophotal twisting for triaxial galaxies orbiting in a cluster potential (see their Figs. 6 and 8). Also, Tenneti et al. (2015) found in cosmological hydrodynamic simulations that the measured IA signal at all spatial separations becomes larger when defining galaxy shapes and orientations in a way that emphasizes the outer parts of the galaxy light profile.

Observationally, since the isophotal shape traces the outermost part of the light profile, the measurement based on isophotal shapes should detect the strongest SA signals, followed by de Vaucouleurs and re-Gaussianization shapes, if isophotal twisting is occurring at a significant level. Singh & Mandelbaum (2016) detect a stronger IA amplitude with isophotal shapes than with re-Gaussianization shapes at large separations ($\gtrsim 5\text{Mpc}$). After considering possible systematic errors, they conclude that this difference most likely originates from isophotal twisting.

In this work, since we focus particularly on galaxies in cluster environments, we need to reassess whether systematics may be contributing in a significant way to the measured MAPADs between the two shape measurement methods compared to what was found in Singh & Mandelbaum (2016). Only after doing so can we draw conclusions about possible detections of isophotal twisting.

The effect of isophote twisting should be more intense for galaxies in a stronger gravitational field. Thus we expect to detect a larger MAPAD for satellites located physically closer, not just looked closer in projection, to the centers of clusters. Therefore, in Fig. 12, we make similar plots for redMaPPer members (teal green circles) as that shown in Fig. 11, but change the x-axis from sky separation to physical projected separation. We process similar noise estimation as what we have done in Fig. 10, i.e. by reweighting non-cluster field galaxies to have similar z , m_r , and ellipticity distributions as that of redMaPPer members, but now operate

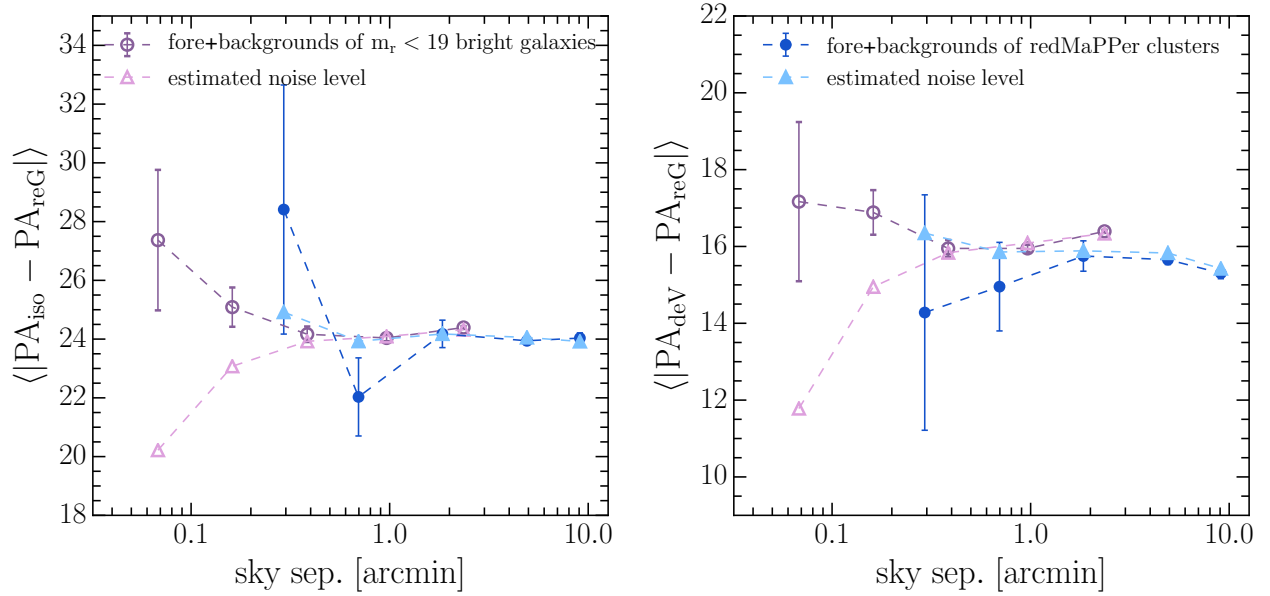


Figure 10. Left panel: mean absolute PA differences (MAPAD) between isophotal and re-Gaussianization shapes as a function of projected angular separation on the sky for galaxies that are in the foreground and background of $m_r < 19$ non-cluster field bright galaxies (purple open circle), and for galaxies in the foreground and background of redMaPPer clusters (dark blue filled circle). The lighter color points shown with triangular symbols indicate the estimated $\langle |PA_{\text{iso}} - PA_{\text{reG}}| \rangle$ contribution from noise (see the text for details). Right panel: similar to the left panel but for the MAPAD between de Vaucouleurs and re-Gaussianization shapes, $\langle |PA_{\text{deV}} - PA_{\text{reG}}| \rangle$. As shown, the MAPAD increases toward small sky separation.

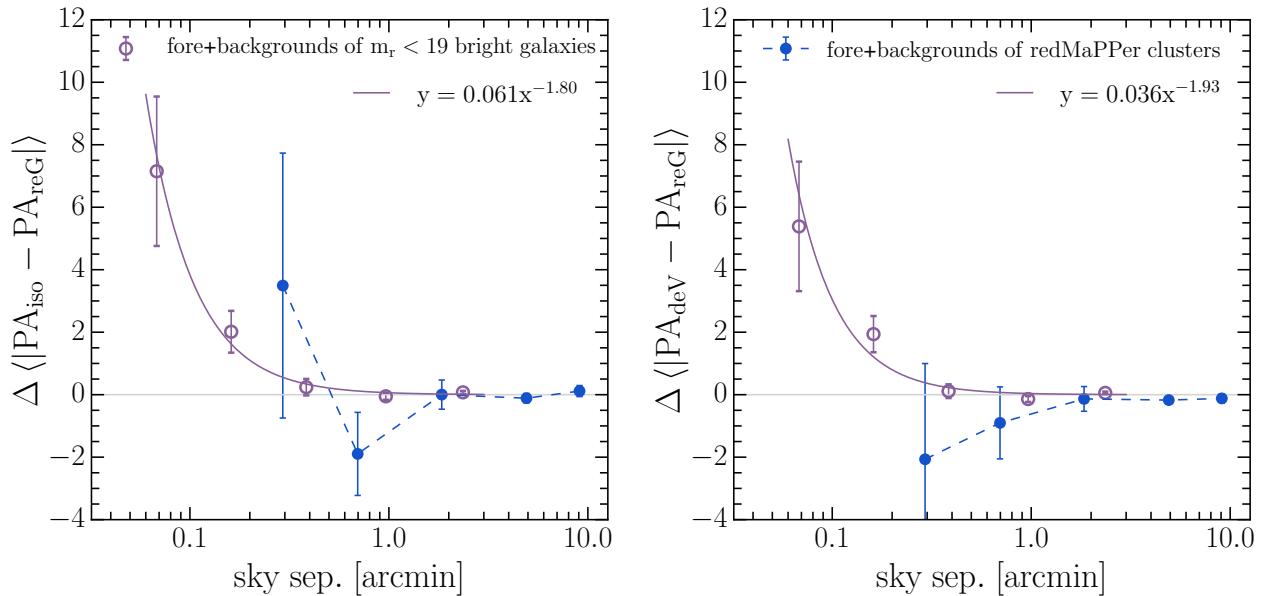


Figure 11. Left panel: Excess of mean absolute PA differences (MAPAD) between isophotal and re-Gaussianization shapes caused by bright neighbor or crowded field systematics as a function of projected angular separation on the sky, for galaxies in the foreground and background of $m_r < 19$ (purple open circle) and for galaxies in the foreground and background of redMaPPer (blue filled circle). Right panel: similar to the left panel, but for the excess of MAPAD between de Vaucouleurs and re-Gaussianization shapes. As shown, the level of bright neighbor and crowded field systematics increases toward small sky separation bins. The fitted models (see Eq. 11) between $\Delta \langle |PA_{\text{iso/deV}} - PA_{\text{reG}}| \rangle$ and sky separation are provided in the legend with $x =$ sky separation measured in arcmin and $y = \Delta \langle |PA_{\text{iso/deV}} - PA_{\text{reG}}| \rangle$.

it in bins of physical projected separation. After the removal of noise, the values of y-axis shown in Fig. 12 should be caused largely by bright neighbor and crowded field systematics, as well as physical isophote twisting effects. The left panel of Fig. 12 is the excess of MAPAD between isophotal and re-Gaussianization shapes, while the right panel plots that between de Vaucouleurs and re-Gaussianization shapes. In the following, we will first try to estimate how much of the excess MAPAD is contributed by the bright neighbor systematic, and then based on that we can judge whether there is leftover isophotal twisting signal.

To estimate what fraction of the excess MAPAD in Fig. 12 is due to the bright neighbor systematic, we apply the following procedure: for each central-satellite pair of redMaPPer member, we use its projected sky separation as input in the derived best-fitting $\Delta\langle|PA_{\text{iso/deV}} - PA_{\text{reG}}|\rangle$ –(sky separation) relation (in the form of Eq. 11) shown in Fig. 11 to estimate the level of systematics in cluster field. Next, we take averages for all central-satellite pairs in each physical r bin. The solid purple line in Fig. 12 indicates the resulting estimated contribution due to bright neighbor systematics. We observe that at the smallest r bin, the bright neighbor systematic could potentially contribute more than 50% of the measured $\Delta\langle|PA_{\text{iso/deV}} - PA_{\text{reG}}|\rangle$. However, the actual level of bright neighbor systematic in cluster environments could be larger, since the central galaxies have (on average) brighter apparent magnitudes than the sample of non-centrals used to estimate the bright neighbor systematic.

Roughly, the remaining differences in the y-axes between the green dashed and purple solid lines are contributed by real physical isophote twisting signal and the crowded field systematic (for which we lack a good estimate). Residual bright neighbor systematic error may also play a role since the average apparent magnitude of cluster central galaxies is brighter than that of the galaxy sample used to estimate the bright neighbor systematic. Unfortunately, we have no good way to empirically estimate the crowded field systematic more accurately, due to the small size of the foreground and background samples in cluster fields. Simulation pipelines associated with future large surveys may be a better tool to estimate and remove various sources of systematic contamination and provide constraints on isophote twisting effects in cluster environments.

6 THE DEPENDENCE OF SATELLITE ALIGNMENT ON THE SELECTED PREDICTORS

In Sec. 4, we apply linear regression analysis and apply the model averaging technique to identify predictors that have a significant influence on the variation of the SA signal (as summarized in Tables 5, 6 and 7 for different shape measurements). We now address possible reasons for the observed relationship between ϕ_{sat} and these selected predictors.

6.1 Dependence on satellite luminosity

As shown in Figs. 6a and 7b, we found that satellite $^{0.1}Mr$ has a very significant influence on the SA signal, with more

luminous satellites being more likely to have their long axes oriented toward their host central galaxies.

Our result is consistent with the observation of Hung & Ebeling (2012). Based on high quality HST/ACS data for shape measurement they also detected a statistically significant trend for the dependence of $\langle\phi_{\text{sat}}\rangle$ on satellite luminosity (see their Fig. 6) for members in 12 X-ray clusters at $z \sim 0.5\text{--}0.6$.

Based on N -body simulations, Pereira et al. (2008) reported that there is no apparent dependence of subhalo alignment signals on the subhalo mass (see their Fig. 3). In a cosmological hydrodynamic simulation, Tenneti et al. (2014) found that the misalignment between a galaxy’s own DM subhalo and its luminous component becomes larger for less massive galaxies. Therefore, the observed relationship between $\langle\phi_{\text{sat}}\rangle$ and satellite luminosity may be due to this misalignment dependence on luminosity. For faint galaxies, which are typically less massive, they appear to be more randomly oriented because their luminous components are not good tracers of the orientation of their own DM halos.

6.2 Dependence on satellite-central distance

Satellite-central distance is another significant factor determining the strength of the SA effect, with satellites located closer to their centrals having a stronger SA signal. Many previous observational studies that have reported detections of SA also found dependence of $\langle\phi_{\text{sat}}\rangle$ on satellite-central distance (Pereira & Kuhn 2005; Agustsson & Brainerd 2006; Faltenbacher et al. 2007; Siverd et al. 2009; Hung & Ebeling 2012).

The satellite-central distance dependence naturally reflects the fact that SA is triggered by tidal forces from the DM potential of the host halo. Hence, the strength of the tidal force would be stronger for satellites located closer to the central region of the host halo. However, as discussed in Sec. 5.2, part of this trend could come from bright neighbor and crowded field systematics, especially for galaxies located near the cluster central region.

From the simulation side, where this radius-dependence can be measured to small scales without observational systematics, Pereira et al. (2008) showed that the relationship between the subhalo SA signal and satellite-central distance is actually non-linear. As shown in their Fig. 4, the SA signal first rises gradually when satellites are closer to cluster center, peaks at around 0.5 times the virial radius, then decreases again toward the center. This is because when falling into the cluster along an eccentric orbit, a subhalo’s orbiting speed becomes too fast for the tidal torquing to be effective at the orbital pericenter, so the alignment cannot keep up with the satellite subhalo’s own motion (see Fig. 8 of Pereira et al. 2008), leading to the decrease in SA signal at very small radius (see also discussion in Sec. 6 of Kuhlen et al. 2007).

6.3 Dependence on satellite ellipticity

We identified a statistically significant SA signal dependence on satellite ellipticity, with rounder satellites exhibiting a stronger tendency to radially point toward their cluster central galaxy. Since it is difficult to accurately determine the PA of a satellite with a round shape, we divide our samples

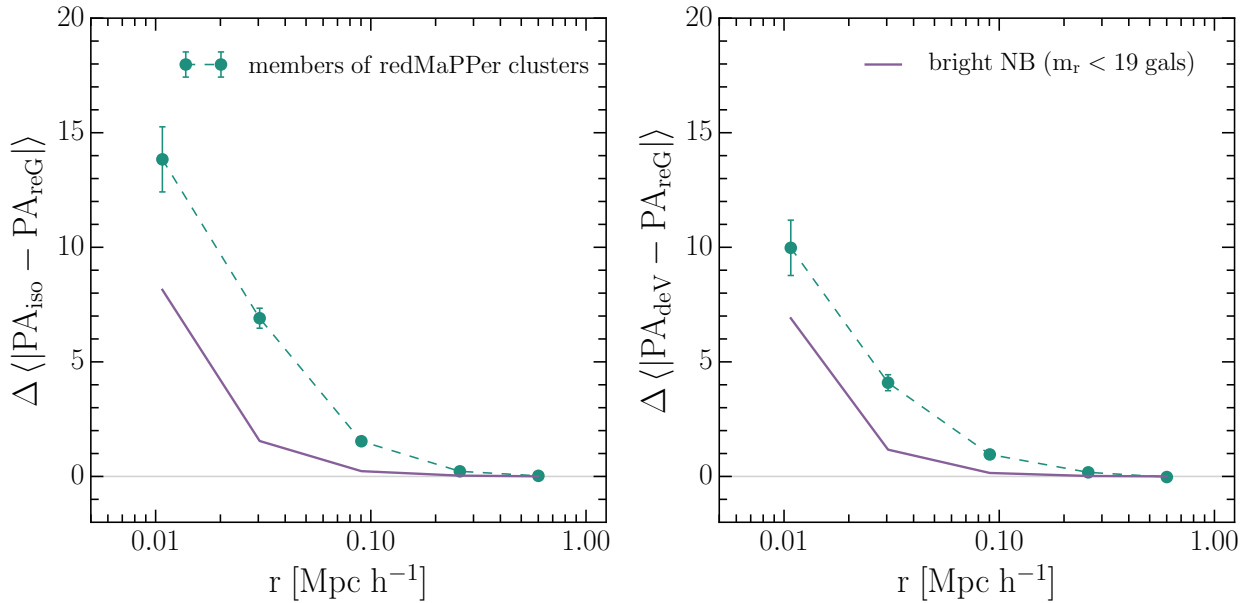


Figure 12. Left panel: Excess of mean absolute PA differences (MAPAD) between isophotal and re-Gaussianization shapes, $\Delta\langle|PA_{\text{iso}} - PA_{\text{reG}}|\rangle$, as a function of projected physical separation for members in redMaPPer clusters (teal green circles). Right panel: similar to the left panel but with $\Delta\langle|PA_{\text{dev}} - PA_{\text{reG}}|\rangle$ in the y-axis. The purple line is the estimated level of bright neighbor systematic derived using the best-fitting models shown in Fig. 11. We observe that at the smallest r bin, the bright neighbor systematic could potentially contribute more than 50% of the measured $\Delta\langle|PA_{\text{iso/dev}} - PA_{\text{reG}}|\rangle$. Roughly, the remaining differences in the y-axes between the green dashed and purple solid lines are contributed by real physical isophote twisting signal and the crowded field systematic (for which we lack a good estimate), and probably some residual bright neighbor systematic due to the fact that the average apparent magnitude of cluster central galaxies is brighter than that of the galaxy sample used to estimate the bright neighbor systematic.

into two ellipticity bins at the boundary of 0.2, and see if the resulting correlation is still strong enough that satellite ellipticity can be selected as an important indicator of the SA effect through the variable selection process. Our result is that this quantity is still selected as a feature predictor. Fig. 13 plots the $\langle\phi_{\text{sat}}\rangle$ value in bins of satellite ellipticity. We see that the net SA signal is fairly strong for satellites with ellipticity < 0.2 (Fig. 13b), and that the detected positive correlation is still quite significant for satellites with ellipticity ≥ 0.2 (Fig. 13c).

According to Pereira & Bryan (2010), for galaxies orbiting in cluster potentials, their stellar components tend to become more spherical with time (see their Fig. 18). Also it takes time for satellites to become tidally locked and pointing radially toward central. We propose that the observed correlation between $\langle\phi_{\text{sat}}\rangle$ and the ellipticity of satellites reflects this physical picture.

6.4 Dependence on the $fracDeV$ parameter

In the work of Siverd et al. (2009), based on a catalog of group-mass systems, they have studied the effect of $fracDeV$, an indicator of a galaxy’s bulge fraction, on the SA signal. They reported that the level of SA strength is most strongly dependent on the $fracDeV$ parameter. To compare with their result, we have added $fracDeV$ into our parameter pool for use during the variable selection process.

Our analysis also showed that $fracDeV$ is a statistically-significant predictor for the satellite alignment effect, with de Vaucouleurs profile-dominated (higher bulge fraction) galaxies having stronger SA signal compared to galaxies with ex-

ponential dominated-profile (higher disk fraction). As shown in the $\phi_{\text{sat}}-fracDeV$ plots of Figs. 6d and 7e, the observed SA signal is mostly coming from satellites with high $fracDeV$ values.

Typically a galaxy with higher luminosity, rounder shape, and redder color tends to have a higher bulge fraction, and thus higher $fracDeV$. Therefore, it is important to ensure that the dependence between ϕ_{sat} and $fracDeV$ is not caused by correlations of $fracDeV$ with other parameters. (Although linear regression is a useful tool to break out degeneracies among parameters, since SA is a weak signal, we still need to pay extra attention on the possible degeneracy issue.) To check whether $fracDeV$ is a representative parameter with its own distinct effect on $\langle\phi_{\text{sat}}\rangle$, we construct five subsamples by excluding satellites of the top 20% most luminous, smallest satellite-central distance, roundest, and reddest color from the parent DR8 sample pool each time. After that, we can check if the remaining 80% of the satellites still exhibit a significant correlation between $fracDeV$ and ϕ_{sat} . In Fig. 14, we plot the averaged ϕ_{sat} in bins of $fracDeV$ for these five subsample sets. One can see that although excluding these satellite subsets decreases the overall SA signal strength, the trend between $fracDeV$ and $\langle\phi_{\text{sat}}\rangle$ remains similar as in the original full sample. This finding confirms that $fracDeV$ really is a special parameter with its own distinct effect on the SA signal.

We propose that $fracDeV$ is chosen as an important predictor because it encapsulates information about the importance of angular momentum in the dynamics of each galaxy. It has been observed that SA signal only appears in samples of red bulge-dominated galaxies, while blue disk-

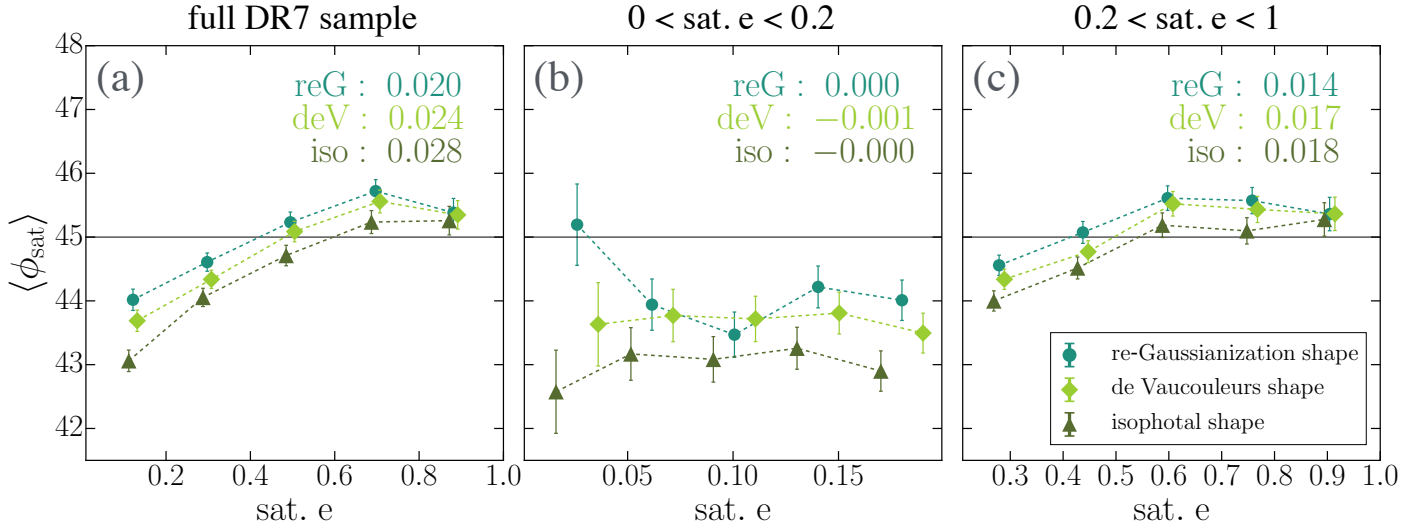


Figure 13. The averaged SA angle, $\langle \phi_{\text{sat}} \rangle$, in bins of satellite ellipticity. The left panel shows all satellites in our DR7 footprint sample; the middle panel shows only satellites with ellipticity < 0.2 , while the right panel shows satellites with ellipticity ≥ 0.2 . The correlation coefficients between ϕ_{sat} and satellite ellipticity measured in various shapes are provided in the upper right corner for each of subsamples. We see the observed significant trend of positive correlation in the full satellite sample is still there for satellites with ellipticity ≥ 0.2 , whose PA (and thus ϕ_{sat}) measurements are more robust.

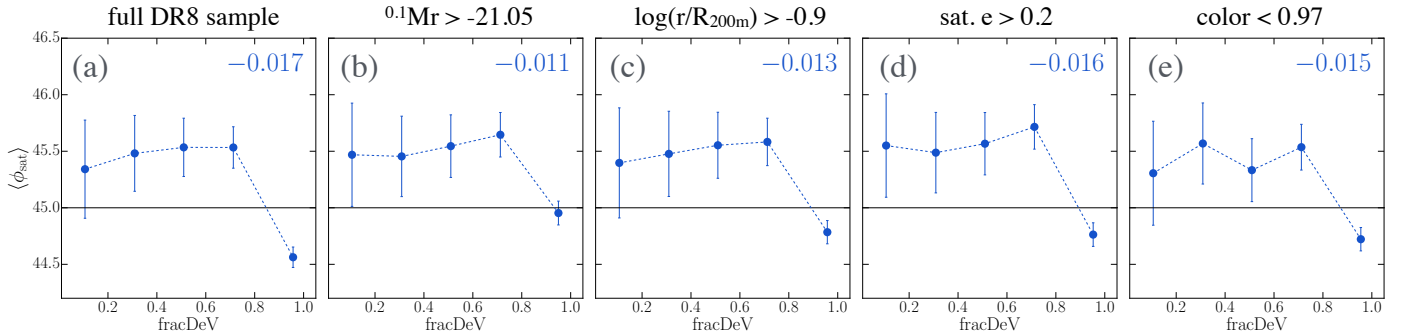


Figure 14. The averaged SA angle, $\langle \phi_{\text{sat}} \rangle$, in bins of fracDeV for different subsamples of the redMaPPer satellites as indicated in the title of each plot. The correlation coefficient between ϕ_{sat} and fracDeV for each subsample is shown in the upper right corner. After excluding part of satellites with properties that correlate with fracDeV , the correlation trend between fracDeV and ϕ_{sat} still remains similar as the original full sample. This confirms that fracDeV as its own distinct effect on the SA signal.

galaxies generally have random orientation within clusters (see e.g. Pereira & Kuhn 2005; Faltenbacher et al. 2007; Siverd et al. 2009 based on SDSS isophotal shapes and Hung & Ebeling 2012 based on high quality HST images). Since material in disks has higher angular momentum compared with that in bulges, it becomes less effective to torque disks to align with the surrounding tidal field. According to the N -body simulation results of Pereira & Bryan (2010), galaxies with initial figure rotation generally take longer to become radially aligned than non-rotating galaxies (see their Sec 5.5). Tenneti et al. (2016) also found using cosmological hydrodynamic simulations that the misalignment angle between disk galaxies with the shape of their host DM subhalos is larger compared with ellipticals. In that case, they used an angular-momentum based discriminator for disk vs. elliptical galaxies, so again fracDeV should be relevant.

We remind the readers that our work only includes fairly red galaxies, since the redMaPPer members are selected based on the red-sequence method. This may lead to the result that fracDeV (tracing angular momentum) appears to be a more important predictor than color (which directly reflects the gas content of a galaxy). However, based on hydrodynamical simulations, Debattista et al. (2015) pointed out that “gas” is a key factor affecting the degree of misalignment between a disk galaxy and its own subhalo. A red, gas poor disk can have a stable orientation governed by halo torques, but when there is gas cooling onto a disk, the blue disk could have arbitrary orientations set by the balance between halo torques and angular momentum of the ongoing gas accretion.

6.5 Dependence on central galaxy alignment angle θ_{cen}

For de Vaucouleurs and isophotal shapes, we detected a positive correlation between ϕ_{sat} and θ_{cen} , with satellites located closer to the central galaxy major axis direction showing a stronger SA signal.

In Paper I, we have explored the angular segregation of satellites in redMaPPer clusters and concluded that the angular segregation may be due to 1) preferential infall of satellites along the filamentary structure aligned with the large-scale primordial tidal field (see Paper I Sec. 6.1) or 2) the newly-established local tidal field produced by the current configuration of satellites which torques centrals to align (see Paper I Sec. 7.3). The observed dependence of ϕ_{sat} on θ_{cen} can also be explained based on the above two scenarios. Assuming that a central galaxy is aligned with its most dominant primordial tidal field, since many satellites are fed into clusters along this direction, some satellites located near the edge of the cluster may still remember their original orientations along this primordial tidal field because of their relatively late entrance into the clusters. Thus, for satellites with small θ_{cen} , it is natural that they will point radially toward central galaxy (Faltenbacher et al. 2008). For the second scenario, if later dynamical evolution has changed the central galaxy's orientation to align with its newly established local tidal field, satellites near cluster central region would also show tendency to align along this tidal field, especially those located at small θ_{cen} , forming a local filamentary structure. Note it is likely that the later local tidal field still follows the direction with its primordial large-scale tidal field.

One way to check the above scenarios is to look at the correlation between θ_{cen} and ϕ_{sat} for satellites at small and large satellite-central separations, as plotted in Fig. 15. We observe that there is almost no signal at the largest $\log(r/R_{200\text{m}})$ bin (Fig. 15d). The correlation is mostly driven by satellites at small $\log(r/R_{200\text{m}})$ bin (Fig. 15b). Thus if the detected correlation is real, then the local tidal field is the most likely cause for the correlation between θ_{cen} and ϕ_{sat} .

Besides the physical origin, the correlation between θ_{cen} and ϕ_{sat} could be induced by systematics. At small satellite-central distances, ϕ_{sat} measurements based on de Vaucouleurs and isophotal shapes may suffer from bright neighbor systematic (see Sec. 5.2.2) due to the central galaxies' extended light profiles. Satellites located on the major axes directions of the centrals would be more strongly affected by this systematic. This may be the reason why θ_{cen} is identified as an important predictor only in de Vaucouleurs and isophotal shape measurements. It therefore remains interesting to check whether we can detect robust dependence between θ_{cen} and ϕ_{sat} , especially at small scale, using simulation data in the future.

6.6 Dependence on redshift

For the isophotal shape measurements, we observed that there is stronger SA for satellites at lower redshift. As shown in Fig. 7f, the correlation coefficient between z and $\langle\phi_{\text{sat}}\rangle$ is very small (0.002), but the correlation is still identified using our variable selection procedure.

However, we suspect that the correlation detected in

isophotal shapes here may be dominated by systematics. For a galaxy at lower redshift, its 25 mag/arcsec² isophote traces a larger area on the sky, and thus would have more fake alignment signal from bright neighbor and crowded field systematics (see Sec. 5.2.2). Besides, the correlation coefficients observed between ϕ_{sat} and z measured in re-Gaussianization and de Vaucouleurs shapes are both negative, meaning that satellites at higher redshift show stronger SA signal (although not a strong enough dependence to be identified through our variable selection procedure).

Comparing with other observational work, Hao et al. (2010) also observed an increase of the SA signal toward lower z based on isophotal shape, but detected no SA signal across all redshift bins using de Vaucouleurs shapes. Schneider et al. (2013) reported stronger SA at higher redshift for early-type galaxies in groups based on 2D Sersic model shape measurements.

From the simulation side, Pereira et al. (2008) found that the SA strength increases steadily with time for all of their simulated clusters (see their Fig. 5), suggesting that IA strength within the one-halo regime requires time to develop. This trend is inconsistent with the current best theoretical model for IA of galaxies at large scales. The linear alignment model (Catelan et al. 2001; Hirata & Seljak 2004) suggests that IA stems from the primordial tidal field at the time when galaxies form. This implies that later merging or baryonic processes of galaxy evolution may weaken this primordial signal, as shown in the N-body simulation work of Hopkins et al. (2005), who found that the strength of cluster alignments (not galaxy alignments within clusters) decreases at later times.

Currently, our technique is not good enough yet to completely demonstrate proper removal of systematics contamination and measure the evolution of SA signals with redshift robustly. Future exploration on the dependence of SA particularly with redshift is important in a sense that it may have different theoretical origin compared with current large-scale linear alignment model, which needs to be investigated to properly extend the linear alignment model down to smaller scale (see e.g. Schneider & Bridle 2010 for smaller scale IA modeling).

7 SUMMARY

In this work, we investigate the radial alignment of satellites in redMaPPer clusters based on three different shape measurement methods: re-Gaussianization, de Vaucouleurs and isophotal shapes. We compare the observed SA signals among these measurements, and explore possible systematic effects. To identify the predictors that are relevant to the variation of the SA signal, we perform linear regressions on all possible models and apply the model averaging technique on a total of 17 physical parameters related to satellite, central galaxy, and cluster properties (see Table 2), and quantify the significance of their relationship with the satellite alignment angle, ϕ_{sat} .

Our main results are summarized as follows:

(i) Based on re-Gaussianization shape measurements, which puts more weight on a galaxy's inner light profile, we do not detect any convincing SA signal in the overall $p_{\text{mem}} > 0.55$ satellite population of redMaPPer clus-

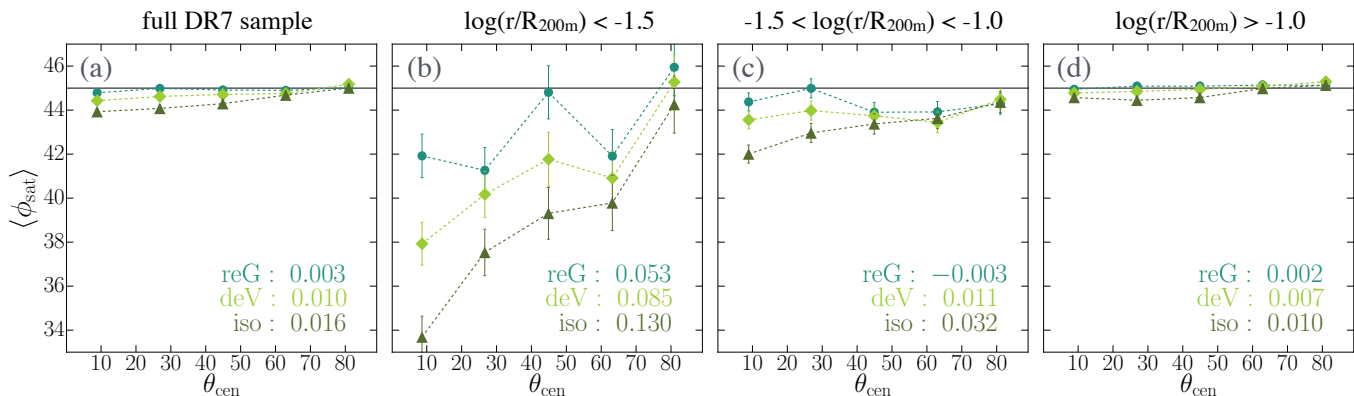


Figure 15. The relationship between $\langle \phi_{\text{sat}} \rangle$ and θ_{cen} for the DR7 footprint sample in different satellite-central separation bins as indicated in the title of each plot. The correlation coefficients between ϕ_{sat} and θ_{cen} measured in various shapes are provided in the upper right corner for each of subsamples. We see that the originally observed significant correlation in the full sample is dominated by satellites located closer to cluster central region.

ters (Fig. 2). However, a statistically significant SA signal is observed for the entire sample when using de Vaucouleurs shapes, and the overall SA strength reaches to its strongest level in isophotal shape, which traces the outermost light profile of a galaxy (Fig. 4).

(ii) Despite the lack of detection of satellite alignments for the entire sample, there are nonetheless distinct sub-populations that carry highly significant satellite alignments signals when measuring using re-Gaussianization. The SA strength is strongest for satellites with higher luminosity, located closer to their central galaxies, with smaller ellipticity, and have higher bulge fraction in the light profiles. (Fig. 6). We also find that satellites located closer to the major axis directions of their central galaxies show higher SA signal, when using de Vaucouleurs and isophotal shape measurements for satellite shapes (Fig. 7).

(iii) The selected predictors that show significant influence on the SA effect highlight the roles of tidal torquing mechanism, the primordial pre-infall alignment, the process of violent relaxation in clusters, and the angular momentum of galaxies in causing the observed SA dependences.

(iv) We discuss possible factors that could cause the observed different strength of SA among these three shape measurement methods (Fig. 8), provide an estimate of the noise level and discuss contributions from systematics and physical isophote twisting effect.

Over the past decade, there has been some disagreement in the literature regarding the existence and strength of the SA effect. Here we report detections of SA phenomenon based on a well-understood shape measurement method using nearly 10^4 clusters, which provides great statistical power in constraining SA. We identify the regions of parameter space where SA signals become significant, which in some cases can explain previous reported non-detections (e.g., in measurements dominated by satellites in the regions of parameter space where we also find no significant detection of SA). Our results will be useful in improving IA modeling at small scale, for example by building a more realistic halo model of intrinsic alignments (building on work by Schneider & Bridle 2010), and further helps constrain systematics from IA in weak lensing analysis. We also discuss

possible physical origins of the SA signal based on the galaxy and cluster properties that most strongly predict it, and point out directions for future work with even larger cluster samples that are becoming available with next-generation imaging surveys.

ACKNOWLEDGEMENTS

We thank Eric Baxter for providing galaxy concentration parameter used in the work, and Sukhdeep Singh for helpful comments and discussions. We also thank Sivaraman Balakrishnan for sharing his view on various model selection criteria. This work was supported by the National Science Foundation under Grant No. AST-1313169 and by NASA ROSES 12-EUCLID12-0004.

REFERENCES

- Agustsson I., Brainerd T. G., 2006, *ApJ*, **644**, L25
 Aihara H., et al., 2011, *ApJS*, **195**, 26
 Akaike H., 1998, in , Selected Papers of Hirotugu Akaike. Springer, pp 199–213
 Blazek J., Mandelbaum R., Seljak U., Nakajima R., 2012, *J. Cosmology Astropart. Phys.*, **5**, 041
 Burnham K. P., Anderson D. R., 2003, Model selection and multimodel inference: a practical information-theoretic approach. Springer Science & Business Media
 Catelan P., Kamionkowski M., Blandford R. D., 2001, *MNRAS*, **320**, L7
 Chen Y.-C., et al., 2015, *MNRAS*, **454**, 3341
 Chisari N., et al., 2015, *MNRAS*, **454**, 2736
 Ciotti L., Dutta S. N., 1994, *MNRAS*, **270**, 390
 Dark Energy Survey Collaboration et al., 2016, *MNRAS*, **460**, 1270
 Debattista V. P., van den Bosch F. C., Roškar R., Quinn T., Moore B., Cole D. R., 2015, *MNRAS*, **452**, 4094
 Faltenbacher A., Li C., Mao S., van den Bosch F. C., Yang X., Jing Y. P., Pasquali A., Mo H. J., 2007, *ApJ*, **662**, L71
 Faltenbacher A., Jing Y. P., Li C., Mao S., Mo H. J., Pasquali A., van den Bosch F. C., 2008, *ApJ*, **675**, 146
 Grueber C., Nakagawa S., Laws R., Jamieson I., 2011, *Journal of evolutionary biology*, **24**, 699

- Hao J., et al., 2010, *ApJS*, **191**, 254
- Hao J., Kubo J. M., Feldmann R., Annis J., Johnston D. E., Lin H., McKay T. A., 2011, *ApJ*, **740**, 39
- Hirata C., Seljak U., 2003, *MNRAS*, **343**, 459
- Hirata C. M., Seljak U., 2004, *Phys. Rev. D*, **70**, 063526
- Hirata C. M., Mandelbaum R., Ishak M., Seljak U., Nichol R., Pimblet K. A., Ross N. P., Wake D., 2007, *MNRAS*, **381**, 1197
- Hopkins P. F., Bahcall N. A., Bode P., 2005, *ApJ*, **618**, 1
- Hung C.-L., Ebeling H., 2012, *MNRAS*, **421**, 3229
- Joachimi B., Mandelbaum R., Abdalla F. B., Bridle S. L., 2011, *A&A*, **527**, A26
- Joachimi B., et al., 2015, *Space Sci. Rev.*, **193**, 1
- Kiessling A., et al., 2015, *Space Sci. Rev.*, **193**, 67
- Kirk D., et al., 2015, *Space Sci. Rev.*, **193**, 139
- Kormendy J., 1982, Morphology and dynamics of galaxies; Proceedings of the Twelfth Advanced Course, Saas-Fee, Switzerland, March 29-April 3, 1982 (A84-15502 04-90). Sauverny, Switzerland, Observatoire de Geneve, 1983, p. 113-288., **12**, 113
- Krause E., Eifler T., Blazek J., 2016, *MNRAS*, **456**, 207
- Kuhlen M., Diemand J., Madau P., 2007, *ApJ*, **671**, 1135
- LSST Science Collaboration et al., 2009, preprint, ([arXiv:0912.0201](https://arxiv.org/abs/0912.0201))
- Laureijs R., et al., 2011, preprint, ([arXiv:1110.3193](https://arxiv.org/abs/1110.3193))
- Mandelbaum R., et al., 2005, *MNRAS*, **361**, 1287
- Mandelbaum R., Hirata C. M., Ishak M., Seljak U., Brinkmann J., 2006, *MNRAS*, **367**, 611
- Mandelbaum R., et al., 2011, *MNRAS*, **410**, 844
- Mandelbaum R., Slosar A., Baldauf T., Seljak U., Hirata C. M., Nakajima R., Reyes R., Smith R. E., 2013, *MNRAS*, **432**, 1544
- Massey R., Kitching T., Richard J., 2010, *Reports on Progress in Physics*, **73**, 086901
- Miyazaki S., et al., 2012, *Proc. SPIE*, 8446, 84460Z
- Okumura T., Jing Y. P., Li C., 2009, *ApJ*, **694**, 214
- Pereira M. J., Bryan G. L., 2010, *ApJ*, **721**, 939
- Pereira M. J., Kuhn J. R., 2005, *ApJ*, **627**, L21
- Pereira M. J., Bryan G. L., Gill S. P. D., 2008, *ApJ*, **672**, 825
- Refregier A., Kacprzak T., Amara A., Bridle S., Rowe B., 2012, *MNRAS*, **425**, 1951
- Reyes R., Mandelbaum R., Gunn J. E., Nakajima R., Seljak U., Hirata C. M., 2012, *MNRAS*, **425**, 2610
- Rozo E., Rykoff E. S., 2014, *ApJ*, **783**, 80
- Rozo E., Rykoff E. S., Bartlett J. G., Melin J.-B., 2015a, *MNRAS*, **450**, 592
- Rozo E., Rykoff E. S., Becker M., Reddick R. M., Wechsler R. H., 2015b, *MNRAS*, **453**, 38
- Rozo E., et al., 2016, *MNRAS*, **461**, 1431
- Rykoff E. S., et al., 2012, *ApJ*, **746**, 178
- Rykoff E. S., et al., 2014, *ApJ*, **785**, 104
- Schneider M. D., Bridle S., 2010, *MNRAS*, **402**, 2127
- Schneider M. D., et al., 2013, *MNRAS*, **433**, 2727
- Sifón C., Hoekstra H., Cacciato M., Viola M., Köhlinger F., van der Burg R. F. J., Sand D. J., Graham M. L., 2015, *A&A*, **575**, A48
- Simet M., McClintock T., Mandelbaum R., Rozo E., Rykoff E., Sheldon E., Wechsler R. H., 2017, *MNRAS*, **466**, 3103
- Singh S., Mandelbaum R., 2016, *MNRAS*, **457**, 2301
- Singh S., Mandelbaum R., More S., 2015, *MNRAS*, **450**, 2195
- Siverd R. J., Ryden B. S., Gaudi B. S., 2009, preprint, ([arXiv:0903.2264](https://arxiv.org/abs/0903.2264))
- Smargon A., Mandelbaum R., Bahcall N., Niederste-Ostholt M., 2012, *MNRAS*, **423**, 856
- Spergel D., et al., 2015, preprint, ([arXiv:1503.03757](https://arxiv.org/abs/1503.03757))
- Stoughton C., et al., 2002, *AJ*, **123**, 485
- Tempel E., Guo Q., Kipper R., Libeskind N. I., 2015, *MNRAS*, **450**, 2727
- Tenneti A., Mandelbaum R., Di Matteo T., Feng Y., Khandai N., 2014, *MNRAS*, **441**, 470
- Tenneti A., Singh S., Mandelbaum R., Matteo T. D., Feng Y., Khandai N., 2015, *MNRAS*, **448**, 3522
- Tenneti A., Mandelbaum R., Di Matteo T., 2016, *MNRAS*, **462**, 2668
- Tenneti A., Gnedin N. Y., Feng Y., 2017, *ApJ*, **834**, 169
- Weinberg D. H., Mortonson M. J., Eisenstein D. J., Hirata C., Riess A. G., Rozo E., 2013, *Phys. Rep.*, **530**, 87
- York D. G., et al., 2000, *AJ*, **120**, 1579
- Zhang Y., Yang X., Wang H., Wang L., Mo H. J., van den Bosch F. C., 2013, *ApJ*, **779**, 160
- Zu Y., Mandelbaum R., Simet M., Rozo E., Rykoff E. S., 2016, preprint, ([arXiv:1611.00366](https://arxiv.org/abs/1611.00366))
- de Jong J. T. A., et al., 2015, *A&A*, **582**, A62
- di Tullio G., 1978, *A&A*, **62**, L17
- van Uitert E., Joachimi B., 2017, preprint, ([arXiv:1701.02307](https://arxiv.org/abs/1701.02307))

APPENDIX A: THE CHOICE OF MEMBERSHIP PROBABILITY CUT OF OUR SAMPLE

There are several considerations driving the choice of p_{mem} cut when defining the sample to use for measuring SA. In general, a higher p_{mem} cut would result in a stronger SA signal because brighter and redder satellites tend to have a higher p_{mem} in redMaPPer, and these galaxies are more likely to point radially toward cluster centers. However, raising the threshold in p_{mem} results in a smaller sample size, and thus larger statistical uncertainty. Setting a lower p_{mem} cut would increase the sample size (reduce statistical errors), but also results in a lower signal due to both the inclusion of lower luminosity satellites which carry less signal, and due to the higher contamination rate from non-cluster members. In this appendix, we attempt to estimate the SA signal and noise as a function of the p_{mem} cut. Based on the observed dependences, we can then determine a p_{mem} cut that maximizes the S/N of SA.

Here we define the signal S to be the weighted averaged SA angle over all potential central-satellite pairs indexed i ,

$$S = \langle 45^\circ - \phi_{\text{sat}} \rangle = \frac{\sum_i w_i (45^\circ - \phi_{\text{sat},i})}{\sum_i w_i}, \quad (\text{A1})$$

where w_i is the weighting factor for each central-satellite pair. In practice, we use $w_i = p_{\text{mem},i}$. We shift ϕ_{sat} by 45° such that for pairs with no alignment, their signal $S = 0$. Some of the central-satellite pairs used in our calculation may be contaminated by foreground/background galaxies that are not physically associated with the cluster system. These fake pairs are assumed to contribute nothing to the numerator of Eq. (A1); in other words, we are ignoring the lensing of background galaxies, which would lead to $\langle \phi_{\text{sat}} \rangle > 45^\circ$. We can rewrite Eq. (A1) as

$$S = \frac{\sum_{\text{real pair},j} w_j (45^\circ - \phi_{\text{sat},j})}{\sum_i w_i}, \quad (\text{A2})$$

with the summation in the numerator (indexed j) now including only contributions from real central-satellite pairs. The contaminating pairs do contribute to the denominator, thereby diluting the signal. Under the assumption that the

p_{mem} values in the redMaPPer catalogue represent a correct statistical description of cluster membership (but see Zu et al. 2016), the summation $\sum_{\text{real pair}, j}$ should be statistically equivalent to $\sum_i p_{\text{mem}, i}$. Also, we find that a linear model is a good description for the relationship between the strength of the SA signal ($45^\circ - \phi_{\text{sat}}$) and p_{mem} ⁵.

With these two simplifications and also putting $w_i = p_{\text{mem}, i}$ in Eq. (A2), we conclude that the signal S is described as

$$S \propto \frac{\sum_i p_{\text{mem}, i}^3}{\sum_i p_{\text{mem}, i}}. \quad (\text{A3})$$

The first $p_{\text{mem}, i}$ in the numerator comes from replacing the summation over real central-satellite pairs with the summation over all potential pairs; the second comes from the weight; and the third from the approximation that individual SA signal to lowest order are proportional to $p_{\text{mem}, i}$.

For the noise N , we simply apply standard error of the mean as the level of noise here, i.e. $N = \sigma_{\phi_{\text{sat}}}/\sqrt{N_{\text{eff}}}$. Here the standard deviation of ϕ_{sat} ($\sigma_{\phi_{\text{sat}}}$) is around 26° per p_{mem} bin, while the effective number of central-satellite pairs (N_{eff}) is ranging from 10^4 to 5×10^4 across various p_{mem} bins. Therefore, the variation in the noise on the measurement of the average ϕ_{sat} value with the p_{mem} cut value is mostly driven by the change in N_{eff} . We assume that the noise N is proportional to the Poisson noise on the mean value, defined as

$$N \propto \frac{1}{\sqrt{N_{\text{eff}}}} = \frac{1}{\sqrt{\sum_i p_{\text{mem}, i}}}. \quad (\text{A4})$$

The signal to noise ratio S/N would then be proportional to:

$$S/N \propto \frac{\sum_i p_{\text{mem}, i}^3}{\sqrt{\sum_i p_{\text{mem}, i}}}. \quad (\text{A5})$$

This is a quantity that we can easily calculate for all central-satellite pairs in our catalog, as a function of the lower limit on p_{mem} . The results are shown in Fig. A1. A p_{mem} cut at 0.55 gives the highest S/N , so we adopt this value throughout our analysis.

APPENDIX B: ESTIMATING $\langle \phi_{\text{SAT}} \rangle$ WITH CONTAMINATION FROM BACKGROUND LENSING SIGNAL

In Fig. 6, we saw that there are some subsamples with measured $\langle \phi_{\text{sat}} \rangle > 45^\circ$, meaning that satellites in these data bins show a net preferred tangential alignment signal. Part of the excess may come from lensing of galaxies that are actually in the background, because we allow a p_{mem} cut at 0.55 when

⁵ We have tried fitting the relation between $(45^\circ - \phi_{\text{sat}})$ and p_{mem} with linear, quadratic, and other higher order of power law models. Unfortunately, our data does not have the power to constrain more complicated models very well, so we simply apply the linear model here.

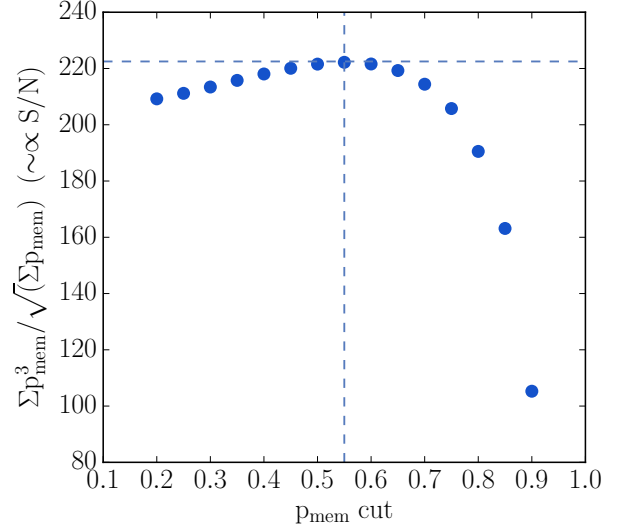


Figure A1. Satellite alignment S/N optimization with different p_{mem} thresholds. The S/N is maximized at p_{mem} cut = 0.55. Note that the absolute normalization of the curve is arbitrary; only the relative changes as a function of the p_{mem} cut are meaningful.

doing our analysis. Here we provide a rough estimate of the degree of this contamination based on the re-Gaussianization shape results⁶.

We begin by defining two quantities: fraction of expected contamination from fake members (f_x) and fraction of expected contribution from true members (f_v). Assuming that the p_{mem} values provide a correct statistical reflection of reality, we can estimate these via summations over all central-satellite pairs with $p_{\text{mem}} > 0.55$, indexed i :

$$f_x = \frac{\sum_i w_i (1 - p_{\text{mem}})}{\sum_i w_i} \quad (\text{B1})$$

$$f_v = \frac{\sum_i w_i (p_{\text{mem}})}{\sum_i w_i} \quad (\text{B2})$$

Here the weighting factor is just p_{mem} , and by definition, $f_x + f_v = 1$.

After f_x and f_v are calculated, we can estimate the predicted value of $\langle \phi_{\text{sat}} \rangle$ due to background contamination by:

$$\langle \phi_{\text{sat}} \rangle_{\text{pred}} = f_v \times 44.92 + f_{\text{back}} f_x \times 46.07 + (1 - f_{\text{back}}) f_x \times 45.0 \quad (\text{B3})$$

Here f_{back} is a free parameter that controls the fraction of contaminating pairs for which the contaminating galaxy is in the background (while $1 - f_{\text{back}}$ is the fraction of contaminating pairs consisting of foregrounds). The predicted $\langle \phi_{\text{sat}} \rangle$ value from each component is taken from that shown in the legend of Fig. 2. For real cluster members, $\langle \phi_{\text{sat}} \rangle = 44.92$; for background pairs $\langle \phi_{\text{sat}} \rangle = 46.07$, while for foregrounds,

⁶ In principle, lensing contamination comes into all shape measurements, but for de Vaucouleurs and isophotal shapes, it is hard to extract the hidden lensing signal due to higher levels of systematics in these shape measurements.

we expect ϕ_{sat} to have $\langle\phi_{\text{sat}}\rangle = 45.0$. The triangular orange data points shown in Fig. 6 are estimated based on setting $f_{\text{back}} = 0.6$. Although here we do not have a good estimation for f_{back} , we find that the derived $\langle\phi_{\text{sat}}\rangle_{\text{pred}}$ are all roughly around 45.1° , insensitive to the setting of f_{back} values ranging from 0.5~1.

This paper has been typeset from a $\text{\TeX}/\text{\LaTeX}$ file prepared by the author.